

# **Turbulent Separated Flow over a Ramp: A Numerical Investigation**

Bono Wasistho and Kyle D. Squires  
Mechanical and Aerospace Engineering Department  
Arizona State University  
P.O. Box 876106  
Tempe, AZ 85287 USA

Prepared with the support of the  
Office of Naval Research  
under Grant No. N00014-98-1-0060



**DISTRIBUTION STATEMENT A**  
Approved for Public Release  
Distribution Unlimited

# REPORT DOCUMENTATION PAGE

Form Approved  
OMB No. 0704-0188

Public reporting burden for this collection of information is estimated to average 1 hour per response, including the time for reviewing instructions, searching existing data sources, gathering and maintaining the data needed, and completing and reviewing this collection of information. Send comments regarding this burden estimate or any other aspect of this collection of information, including suggestions for reducing this burden to Department of Defense, Washington Headquarters Services, Directorate for Information Operations and Reports (0704-0188), 1215 Jefferson Davis Highway, Suite 1204, Arlington, VA 22202-4302. Respondents should be aware that notwithstanding any other provision of law, no person shall be subject to any penalty for failing to comply with a collection of information if it does not display a currently valid OMB control number. PLEASE DO NOT RETURN YOUR FORM TO THE ABOVE ADDRESS.

<b>1. REPORT DATE (DD-MM-YYYY)</b> 12-03-2002		<b>2. REPORT TYPE</b> Final Technical Report	<b>3. DATES COVERED (From - To)</b> Nov 1997-Oct 1999; Mar 2002
<b>4. TITLE AND SUBTITLE</b> <del>A New Two-way Coupling Approach for LES of High Reynolds Number Flows</del>			<b>5a. CONTRACT NUMBER</b>
			<b>5b. GRANT NUMBER</b> N00014-98-1-0060
			<b>5c. PROGRAM ELEMENT NUMBER</b>
<b>6. AUTHOR(S)</b>  Squires, Kyle D.  Wasistho, Bono			<b>5d. PROJECT NUMBER</b>
			<b>5e. TASK NUMBER</b>
			<b>5f. WORK UNIT NUMBER</b>
<b>7. PERFORMING ORGANIZATION NAME(S) AND ADDRESS(ES)</b>  Mechanical and Aerospace Engineering Department, Arizona State University, Tempe, AZ 85287-6106			<b>8. PERFORMING ORGANIZATION REPORT NUMBER</b>  XAA 0045/TE
<b>9. SPONSORING / MONITORING AGENCY NAME(S) AND ADDRESS(ES)</b> Office of Naval Research      ATTN: Patrick Purtell 800 N. Quincy Street            Program Officer Arlington, VA 22217-5660      ONR 333 Ballston Centre Tower One			<b>10. SPONSOR/MONITOR'S ACRONYM(S)</b> ONR
			<b>11. SPONSOR/MONITOR'S REPORT NUMBER(S)</b>

<b>12. DISTRIBUTION / AVAILABILITY STATEMENT</b>  APPROVED FOR PUBLIC RELEASE.
--

20020322 170

<b>13. SUPPLEMENTARY NOTES</b>
--------------------------------

<b>14. ABSTRACT</b> Large Eddy Simulation (LES) and Reynolds-averaged Navier-Stokes (RANS) calculations have been performed of the turbulent flow over a smoothly-contoured ramp. The upstream conditions are prescribed as canonical turbulent boundary layer, obtained from a separate pre-computation. The flow in the primary calculation develops downstream, first experiencing an increase in the surface skin friction due to ramp curvature, then exhibiting a shallow separation with subsequent reattachment on a flat section downstream. The computational domain includes the downstream recovery region, enabling an assessment of model predictions of the recovery process. The turbulence models implemented are the Spalart-Allmaras one-equation model, referred to as S-A throughout (Spalart and Allmaras 1994), V2F (Durbin 1991), and a modified version, referred to as M2VF (Lien and Durbin 1996). Visualizations of the instantaneous flow shows that the separation location fluctuates at a higher frequency than the reattachment location, with the instantaneous reattachment trajectory giving indications of short shedding events. The mean velocities collapse to the universal log law at about four ramp lengths downstream of the beginning of the curved section whereas the turbulence quantities recover more slowly. The recovery process is not monotonic in that it is governed by decay of the outer layer perturbations and initiation and growth of inner layer following attachment.
---

<b>15. SUBJECT TERMS</b> Large Eddy Simulation, Separated Flows, Recovering Boundary Layers, Reynolds Number Effects
---

<b>16. SECURITY CLASSIFICATION OF:</b>			<b>17. LIMITATION OF ABSTRACT</b>	<b>18. NUMBER OF PAGES</b> 42	<b>19a. NAME OF RESPONSIBLE PERSON</b> Kyle D. Squires
<b>a. REPORT</b>	<b>b. ABSTRACT</b>	<b>c. THIS PAGE</b>			<b>19b. TELEPHONE NUMBER (include area code)</b> (480) 965-3957

## Abstract

Large Eddy Simulation (LES) and Reynolds-averaged Navier-Stokes (RANS) calculations have been performed of the turbulent flow over a smoothly contoured ramp. The upstream conditions are prescribed as a canonical turbulent boundary layer, obtained from a separate pre-computation. The flow in the primary calculation develops downstream, first experiencing an increase in the surface skin friction due to ramp curvature, then exhibiting a shallow separation with subsequent reattachment on a flat section downstream. The computational domain includes the downstream recovery region, enabling an assessment of model predictions of the recovery process. The turbulence models implemented are the Spalart-Allmaras one-equation model, referred to as S-A throughout, (Spalart and Allmaras 1994), V2F (Durbin 1991), and a modified version, referred to as MV2F (Lien and Durbin 1996). Visualizations of the instantaneous flow shows that the separation location fluctuates at a higher frequency than the reattachment location, with the instantaneous reattachment trajectory giving indications of short shedding events. The mean velocities collapse to the universal log law at about four ramp lengths downstream of the beginning of the curved section whereas the turbulence quantities recover more slowly.

The recovery process is non-monotonic in that it is started by a decay process and followed by a rebound process. The outer layer is more dominant in the former while the inner layer is more dominant in the latter. The commonly observed drop in the Reynolds shear stress directly after reattachment is believed to be typical for geometry induced separation, rather than for flows with a fixed separation location. Upstream of separation the predictions from all the models show good agreement with measurements. The models, however, respond differently to the separation. As far as mean and integral quantities are concerned, S-A predictions are closest to LES results. Downstream of separation, V2F yields a better agreement with S-A and LES than its modified version, which exhibits a distinctly late reattachment and slower recovery. The slow recovery of S-A in skin friction predictions and V2F mean velocities and the over-prediction of the backflow in the separation region seem analogous to related predictions in reattaching flows. On the turbulence quantities, V2F yields a better agreement with LES than the other models. All the models, however, fail to follow closely follow the dynamics of the inner layer in the rebound process.

# Contents

<b>Abstract</b>	<b>i</b>
<b>Contents</b>	<b>ii</b>
<b>1 Introduction</b>	<b>1</b>
<b>2 Numerical Method</b>	<b>3</b>
2.1 Fractional Step Method . . . . .	3
2.2 RANS Models . . . . .	4
2.3 LES Model . . . . .	6
<b>3 Flow Configuration and Validation</b>	<b>8</b>
<b>4 Results</b>	<b>9</b>
4.1 Mean and Integral Quantities . . . . .	9
4.2 Turbulence Quantities . . . . .	12
<b>5 Conclusion</b>	<b>14</b>

# 1 Introduction

The study of turbulent separation and reattachment has attracted many researchers due to its frequent occurrence in practical flows. While our understanding of the characteristics of turbulent boundary layers up to separation has been fairly well developed, our knowledge on the flow in the separation and recovery region is less mature. A closed separation, although mostly undesired, often inevitably occurs in many flows of hydrodynamic and aerodynamic interest. It is useful, therefore, to develop a more comprehensive understanding of the reattachment and recovery processes in order to eventually control these processes, improve device performance, etc. Moreover, reattachment and recovery processes forms a stringent test for engineering turbulence models, an attractive aspect of the present flow being the detailed set of measurements available for model assessment.

Quantitative information on the characteristics of turbulent boundary layers up to separation has been gathered for several years, e.g., the work leading to Stratford's criterion on flat plate turbulent boundary layer separation (Stratford 1959a, b), among others. Measurement of adverse pressure gradient (APG) flows by Simpson *et al.* (1977) showed that the universal log law is maintained until quite close to separation. Perry and Schofield (1973), Yaglom (1979) and Durbin and Belcher (1992) provided an outer-layer scaling law that is applicable in APG flows approaching separation. Measurements from Alving and Fernholz (1995) yields a better collapse using the Perry-Schofield coordinates compared to Yaglom (1979) or Durbin and Belcher (1992). The outer layer profile shape based on the latter was given by Dengel and Fernholz (1990).

A great deal of the knowledge on separating flows and on the recovery process after reattachment is up to date qualitative. The structure of a separating turbulent boundary layer in a divergent channel was considered by Simpson *et al.* (1981). Measurements on a backward facing step (BFS) were obtained by, among others, Bradshaw and Wong (1971) and Adams and Johnston (1988). Bradshaw and Wong (1971) proposed a model for reattachment based on the splitting of the reattaching flow into the upstream and downstream directions. Adams and Johnston suggested that the mean flow in the recirculation region from the wall out to the peak of the backflow has laminar-like features despite the high level of fluctuating motion. Recently, DNS results on a separated turbulent boundary layer created by blowing and suction was provided by Na and Moin (1998), which showed a similarity of the kinetic energy budget in the separation region to that of a plane mixing layer. In the backward facing step the maximum Reynolds shear stress decreases after reattachment (e.g., Kim *et al.* 1980, Le *et al.* 1997), but this attenuation is delayed in turbulent separations due to the APG (see Driver 1991, Na and Moin 1998, Alving and Fernholz 1996). It is, however, unclear whether this difference is more affected by the geometry or by the difference in the character of separation where it is fixed in BFS flows but fluctuates in APG-induced separations.

Though details on the separation processes governing many flows remains incomplete, another topic of considerable interest is downstream recovery following reattachment. This is probably due in part to the fact that many of the features of the recovering boundary layer following reattachment are qualitatively independent of the upstream history of the flow (Castro and Epik 1998). There are, however, issues that seem to be conflicting and deserve clarification. Smits and Wood (1985)

reported in their review that the recovery of a boundary layer after a perturbation is initiated from the wall by the formation of an internal layer which grows outward as the shear layer travels downstream. This is in accordance with the shorter response time of the inner layer compared to the outer layer (Smits and Wood 1985). The study of Alving and Fernholz (1996) on a mild separation of a turbulent boundary layer suggests, on the contrary, that the recovery process occurs largely in the outer layer. Castro and Epik (1998) also concluded that the turbulence structure in the inner layer develops no more quickly than the outer layer and that the overall recovery rate is determined by the latter.

In the present study we consider a turbulent separation over a smoothly contoured ramp. The geometry is shown in Figure 1, along with contours of spanwise vorticity from a low Reynolds number Large Eddy Simulation. The separation occurs slightly downstream of the onset of curvature with the extent of the reversed-flow region slightly larger than half of the ramp length. As in other reattaching flows, the turbulent motions after reattachment spread over a larger wall normal extent than before separation. This flow is intermediate between the backward-facing step and separation over a flat plate created by an adverse pressure gradient (e.g., as in Na and Moin 1998) in that it contains features specific to each of these two regimes. As in the BFS, the separation over the ramp considered in this study is induced by geometry changes, but the separation location is not fixed by a feature of the geometry, analogous to APG-induced separation flows.

The purpose of this study is two-fold, i.e., first to clarify some physical issues, such as the role of the inner and outer layers in the recovery process and the primary factors causing the difference in Reynolds shear stress behavior between BFS and APG flow, and second to compare the predictions from some of the leading turbulence models. To achieve the first objective, the computational approach is based on LES using the dynamic eddy viscosity model (Germano *et al.* 1991). For the second objective, the turbulence models utilized are the one-equation Spalart-Allmaras (1994) model, the four-equation  $\overline{v^2}$ - $f$  of Durbin (1991), and its modified version which is a computationally more efficient version (see Lien and Durbin 1996). The Spalart-Allmaras model is referred to as S-A throughout,  $\overline{v^2}$ - $f$  as V2F, and the modified version as MV2F.

Menter (1996) compared the S-A model to the experimental measurements on turbulent separations in both the BFS of Driver and Seegmiller (1985) and APG measured by Driver (1991). In both cases, S-A under-predicts the skin friction following reattachment and over-predicts the backflow in the BFS. The V2F models have been applied to prediction of the separated flow over an airfoil (Lien and Durbin 1996, Iaccarino and Durbin 1996) and BFS (Durbin 1995 and Michelassi *et al.* 1996). The predictions of the baseline and modified versions are comparable on the airfoil considered by Lien and Durbin (1996) and in a good agreement with experimental measurements. Compared to the experiment of Driver and Seegmiller (1985) on the high Reynolds number BFS, the predictions from Michelassi *et al.* (1996) on exhibited a slow recovery of the mean streamwise velocity and an over-prediction of the backflow, similar to that shown by the S-A results. The present study is therefore useful to provide some context as to whether such behavior is typical for the turbulence models considered.

The remainder of this report is organized as follows. The governing equations, boundary conditions, and properties of the numerical solver and the RANS turbulence models, and subgrid model for the LES are outlined in Section 2. We present the flow configuration and the validation of

the computational approach in Section 3. The results on the mean flow, integral and turbulence quantities are discussed in Section 4. Finally, we summarize our findings in Section 5.

## 2 Numerical Method

We consider incompressible flows governed by the conservation of mass and momentum,

$$\partial_j u_j = 0, \quad (1)$$

$$\partial_t u_i + \partial_j (u_i u_j) + \partial_i p - \partial_j \sigma_{ij} = 0. \quad (2)$$

The viscous stress tensor  $\sigma$  in the Navier-Stokes equations above is given by,

$$\sigma_{ij} = \left( \frac{1}{Re} + \nu_t \right) S_{ij}, \quad (3)$$

where

$$S_{ij} = \partial_j u_i + \partial_i u_j, \quad (4)$$

is the strain rate tensor. The Reynolds number  $Re$  is based on the boundary layer thickness at the inflow plane and the freestream velocity. The indices vary as  $i, j = 1, 2$  in two dimensions (RANS simulations) and  $i, j = 1, 2, 3$  in three dimensions (LES). The eddy viscosity  $\nu_t$  closes the Reynolds stress term for both RANS and LES.

### 2.1 Fractional Step Method

The governing equations above are solved using the fractional step method (Chorin 1967 and Temam 1979). This method is comprised of three sequential steps. In the first step, an intermediate velocity  $\hat{u}$  is computed from,

$$\frac{\hat{u}_i - u_i^n}{\Delta t} + \beta_0 \partial_j (u_i u_j)^n + \beta_1 \partial_j (u_i u_j)^{n-1} + \partial_j \sigma_{ij} = 0. \quad (5)$$

The Adams-Bashforth method,  $\beta_0 = 3/2$  and  $\beta_1 = -1/2$ , is used for the convective term and the cross derivatives of the viscous terms. The remaining viscous terms are computed using the Crank-Nicholson method. In the last fractional step the resulting intermediate velocity is corrected by the equation,

$$\frac{u_i^{n+1} - \hat{u}_i}{\Delta t} + \partial_i p^{n+1} = 0. \quad (6)$$

Prior to performing this correction the pressure  $p$  is computed by solving the Poisson equation,

$$\partial_{ii} p^{n+1} = \frac{1}{\Delta t} \partial_i \hat{u}_i, \quad (7)$$

which is obtained by taking the divergence of (6) and substituting the divergence-free constraint for  $u^{n+1}$ . In three dimensions, a fast Fourier transform technique is used in solution of the Poisson

equation for the spanwise direction, which is statistically homogeneous. Periodic conditions are applied along the span. No-slip conditions are satisfied at the lower wall whereas zero normal velocity and zero normal derivative of the streamwise velocity hold along the upper boundary. At the inflow boundary a zero pressure gradient turbulent velocity profiles are imposed, corresponding to the target inflow Reynolds number. All the velocity components are extrapolated at the outflow boundary with an additional correction to ensure the condition of zero flux at the boundaries.

In the present study, we apply the fractional step method on in curvilinear non-orthogonal systems. A more detail formulation of the method can be found in Wu and Squires (1994). The variables are located according to the standard staggered grid arrangement. The spatial discretization is centered and second-order accurate.

## 2.2 RANS Models

Two RANS models are investigated in the present study, the one equation S-A model and a four-equation V2F model. In addition, we consider a modification of the second model, referred to as MV2F.

### a. S-A model

The S-A model of Spalart and Allmaras (1994) solves one transport equation for the eddy viscosity:

$$\partial_t \tilde{\nu} + \partial_j (u_j \tilde{\nu}) = C_{b1} \tilde{\nu}_t \tilde{\Omega} - c_{w1} f_w \left( \frac{\tilde{\nu}}{d} \right)^2 + \frac{c_{b2}}{\sigma} (\partial_j \tilde{\nu})^2 + \frac{1}{\sigma} \partial_j ((\tilde{\nu} + \nu) \partial_j \tilde{\nu}), \quad (8)$$

where  $d$  is the distance to the closest wall. The eddy viscosity is expressed in terms of  $\tilde{\nu}$  as,

$$\nu_t = \tilde{\nu} f_{v1}, \quad f_{v1} = \frac{\chi^3}{\chi^3 + c_{v1}^3}, \quad \chi = \frac{\tilde{\nu}}{\nu}. \quad (9)$$

The production term  $\tilde{\Omega}$  is given by,

$$\tilde{\Omega} = \Omega + \frac{\tilde{\nu}}{\kappa^2 d^2} f_{v2}, \quad f_{v2} = 1 - \frac{\chi}{1 + \chi f_{v1}}, \quad (10)$$

with  $\Omega$  being the absolute value of the vorticity. The blending function  $f_w$  reads as,

$$f_w = g \left[ \frac{1 + c_{w3}^6}{g^6 + c_{w3}^6} \right]^{1/6}, \quad g = r + c_{w2}(r^6 - r), \quad (11)$$

$$r = \min \left( \frac{\tilde{\nu}}{\tilde{\Omega} \kappa^2 d^2}, 10 \right). \quad (12)$$

The coefficients are as follows,

$$\begin{aligned} c_{b1} &= 0.135, \quad \sigma = 2/3, \quad c_{b2} = 0.622, \quad \kappa = 0.41, \\ c_{w1} &= \frac{c_{b1}}{\kappa^2} + \frac{1 + c_{b2}}{\sigma}, \quad c_{w2} = 0.3, \quad c_{w3} = 2, \quad c_{v1} = 7.1. \end{aligned} \quad (13)$$

The eddy viscosity vanishes at the wall as well as at the upper boundary, assuming that the upper boundary is sufficiently far from the lower wall.

### b. V2F model

The V2F model of Durbin (1991) employs the standard  $K - \epsilon$  equations

$$\partial_t K + \partial_j(u_j K) = P - \epsilon + \partial_j \left[ \left( \nu + \frac{\nu_t}{\sigma_K} \right) \partial_j K \right], \quad (14)$$

$$\partial_t \epsilon + \partial_j(u_j \epsilon) = \frac{C_{\epsilon 1} P - C_{\epsilon 2} \epsilon}{T} + \partial_j \left[ \left( \nu + \frac{\nu_t}{\sigma_\epsilon} \right) \partial_j \epsilon \right], \quad (15)$$

with the wall condition,

$$K_w = 0, \quad \epsilon_w \rightarrow 2\nu \frac{K}{y^2}. \quad (16)$$

The rate of turbulence kinetic energy production  $P$  is defined as,

$$P = \nu_t [\partial_j u_i + \partial_i u_j] \text{grad}(\mathbf{u}). \quad (17)$$

The  $v^2$  transport equation reads,

$$\partial_t v^2 + \partial_j(u_j v^2) = Kf - nv^2 \frac{\epsilon}{K} + \partial_j [(\nu + \nu_t) \partial_j v^2], \quad (18)$$

where  $f$  in the  $v^2$  equation is evaluated from,

$$\partial_t f = \frac{1}{T} \left[ \frac{2}{3} + (C_1 - 1) - (C_1 - n) \frac{v^2}{K} \right] + C_2 \frac{P}{K} - f + C_L^2 l^2 \partial_{jj} f. \quad (19)$$

A pseudo time derivative is used for solving the  $f$  equation in order for the transport equations to have the same structure. The time scale  $T$  and length scale  $l$  are given by,

$$T = \max \left[ \frac{k}{\epsilon}, 6 \left( \frac{\nu}{\epsilon} \right)^{1/2} \right], \quad l^2 = \max \left[ \frac{k^3}{\epsilon^2}, C_\eta^2 \left( \frac{\nu^3}{\epsilon} \right)^{1/2} \right]. \quad (20)$$

In the "standard" V2F model  $n = 1$ , which yields the wall conditions,

$$v_w'^2 = 0, \quad f_w \rightarrow -\frac{(24 - 4n)\nu^2 v^2}{\epsilon_w y^4} = -\frac{20\nu^2 v^2}{\epsilon_w y^4}. \quad (21)$$

Finally, the eddy viscosity is computed using,

$$\nu_t = C_\mu v^2 T. \quad (22)$$

The model constants appearing above are,

$$\begin{aligned} C_\mu &= 0.19, & C_{\epsilon 1} &= 1.3 + 0.25/[1 + (0.5y/l)^2]^4, \\ C_{\epsilon 2} &= 1.9, & C_1 &= 1.4, & C_2 &= 0.3, & C_L &= 0.3, \\ C_\eta &= 70, & \sigma_K &= 1.0, & \sigma_\epsilon &= 1.3. \end{aligned} \quad (23)$$

### c. MV2F model

In addition to the two model outlined above, we test the performance of a modified version of the original V2F model proposed by Lien and Durbin (1996). The modification is merely brought into the model to enhance its numerical stability if applied to certain numerical schemes. In explicit and uncoupled schemes a numerical instability can occur due to the term  $y^4$  in the denominator of (21) for  $f$ . To counter this problem, a modification is made by setting  $n = 6$ . In this way one can apply the condition  $f(0) = 0$  as the wall boundary condition. Moreover,  $C_{\epsilon 1}$  and  $C_{\epsilon 2}$  alter to,

$$C_{\epsilon 1} = 1.55 + \exp(-A_{\epsilon} R_y^2), \quad C_{\epsilon 2} = 1.92, \quad (24)$$

where  $A_{\epsilon} = 0.00285$  and  $R_y = y\sqrt{k}/\nu$ . The other constants which also change are,

$$\sigma_{\epsilon} = 1.5 \quad \text{and} \quad C_L = 0.17, \quad (25)$$

the remaining constants are kept unchanged.

For all the models the derivatives of  $\bar{\nu}$ ,  $K$ ,  $\epsilon$ ,  $v^2$  and  $f$  with respect to the streamwise coordinate is set to zero at the outflow boundary. At each time step the transport equation for  $\bar{\nu}$ ,  $K$ ,  $\epsilon$ ,  $v^2$  and  $f$  are solved using successive over-relaxation until the maximum residuals reduce to machine zero.

## 2.3 LES Model

In LES the Navier-Stokes equations (1)-(2) are spatially filtered. The filtered solution  $\bar{f}$  is related to  $f$  via,

$$\bar{f}(\xi, t) = \int_{\Gamma} G(\xi - \eta) f(\eta, t) d\eta, \quad (26)$$

where  $\xi$  and  $\eta$  are coordinate vectors in the flow domain  $\Gamma$ . For the filter function  $G$  a top-hat filter is implicitly imposed by the numerical approach,

$$G(\mathbf{z}) = \begin{cases} \frac{1}{\Delta^3} & \text{if } |z_i| < \Delta_i/2 \text{ for } i = 1, 2, 3 \\ 0 & \text{otherwise} \end{cases}, \quad (27)$$

where  $\Delta_i$  is the filter width in the  $x_i$ -direction and  $\Delta^3 = \Delta_1 \Delta_2 \Delta_3$ . Throughout,  $\Delta_i$  equals twice the grid spacing in the  $x_i$ -direction. The filter function  $G$  is constrained by the following normalization condition,

$$\int_{\Gamma} G(\mathbf{z}) d\mathbf{z} = 1. \quad (28)$$

Applying the filtering procedure to the Navier-Stokes equations we obtain,

$$\partial_j \bar{u}_j = 0, \quad (29)$$

$$\partial_i \bar{u}_i + \partial_j (\bar{u}_i \bar{u}_j) + \partial_i \bar{p} - \partial_j \left[ \left( \frac{1}{Re} + \nu_t \right) \bar{S}_{ij}(\mathbf{u}) \right] = 0 + \epsilon_v. \quad (30)$$

$\epsilon_v$  is a residual term rising from filtering the viscous term due to the nonlinearity. This term is second order in the filter width as shown by Ghosal and Moin (1995) and therefore can be neglected in our second order accurate discretization. The subgrid-scale eddy viscosity  $\nu_t$  is used to close the residual stress,

$$\tau_{ij} = \overline{u_i u_j} - \bar{u}_i \bar{u}_j = -\nu_t S_{ij}(\bar{\mathbf{u}}), \quad (31)$$

where  $S_{ij}$  is the strain rate tensor of the filtered velocities. Note that formally only the anisotropic part of the turbulent stress,  $\tau_{ij}^a = \tau_{ij} - \delta_{ij} \tau_{kk} / 3$ , is modeled. The present formulation, however, yields the same result for the model coefficient. In the dynamic formulation the eddy viscosity reads,

$$\nu_t = C_d \Delta^2 |S(\bar{\mathbf{u}})| \quad \text{with} \quad |S(\bar{\mathbf{u}})|^2 = \frac{1}{2} S_{ij}(\bar{\mathbf{u}}) S_{ij}(\bar{\mathbf{u}}). \quad (32)$$

$C_d$  is the model coefficient that is dynamically determined using the Germano identity (Germano *et al.* 1991). This identity reads,

$$T_{ij} - \widehat{\tau_{ij}} = L_{ij}, \quad (33)$$

where  $\tau_{ij}$  is the Reynolds stress tensor (31). The hat filter denotes the test filter corresponding to a filter width  $\widehat{\Delta}$ , to distinguish it from the basic filter, denoted by the bar filter, with a filter width  $\Delta$ . The other terms are given by,

$$T_{ij} = \widehat{\overline{u_i u_j}} - \widehat{\bar{u}_i \bar{u}_j}, \quad (34)$$

$$L_{ij} = \widehat{\overline{u_i u_j}} - \widehat{\bar{u}_i \bar{u}_j}. \quad (35)$$

The tensor  $L_{ij}$  can be explicitly calculated from the basic filtered variables  $\bar{\mathbf{u}}$ .

Substituting the subgrid model (31) into the Germano identity yields,

$$C_d M_{ij} = L_{ij}, \quad (36)$$

where

$$M_{ij} = -\widehat{\Delta}^2 |S(\widehat{\mathbf{u}})| S_{ij}(\widehat{\mathbf{u}}) + (\Delta^2 |S(\bar{\mathbf{u}})| S_{ij}(\bar{\mathbf{u}})) \widehat{\phantom{x}}. \quad (37)$$

The notation  $(\widehat{\phantom{x}})$  denotes that the hat-filter is applied to the term between the brackets. The unknown  $C_d$  is calculated by using a least-squares approach following Lilly (1992),

$$C_d = \frac{\langle M_{ij} L_{ij} \rangle}{\langle M_{ij} M_{ij} \rangle}, \quad (38)$$

where the symbol  $\langle \cdot \rangle$  is an averaging operator over the homogeneous direction (in this case the spanwise direction). Formally, only the anisotropic part of  $\tau_{ij}$ ,  $T_{ij}$  and  $L_{ij}$  is included in (31), (35) and (35), respectively. This would result in  $C_d M_{ij} = L_{ij}^a$  in (36). The expression for  $C_d$ , however, remains unchanged as  $M_{ij} L_{ij}^a = M_{ij} L_{ij}$ .

### 3 Flow Configuration and Validation

We consider a Newtonian flow over a ramp at Reynolds number 10400 based on the inflow boundary layer thickness and freestream velocity. The geometry of the ramp is shown in Figure 2 using the ramp length as the characteristic length scale. The inflow boundary is located four ramp lengths upstream of the onset of curvature and the outflow boundary is at 6.5 ramp lengths downstream for the LES. The outlet location for RANS is one ramp length further downstream, merely because it is affordable for RANS to have a longer recovery domain.

The RANS calculations are performed on a grid of  $323 \times 53$  in the  $x$  and  $y$  directions, respectively. We use notation  $x, y, z$  and  $u, v, w$  instead of  $x_i$  and  $u_i$ ,  $i = 1, 2, 3$  from this point for convenience. This grid corresponds to  $\Delta x^+ = 134$  and  $y^+ = 1.44$  at the first grid point from the wall. Grid refinement tests are carried out using a resolution  $338 \times 58$  and  $233 \times 38$ . The two produce nearly the same result as illustrated by the pressure coefficient and the skin friction for the S-A model in Figure 3 and 4. The same conclusion holds for the other models. Therefore, the intermediate grid  $323 \times 53$  is sufficient and is selected for the remaining calculations. The LES grid is  $484 \times 60 \times 101$ , equivalent to  $\Delta x^+ = 80$ ,  $\Delta z^+ = 22$  and  $y^+ = 1.2$  at the first grid point from the wall. This implies that the streamwise velocity and the pressure adjacent to the wall is computed at about  $y^+ = 0.6$  as we follow a staggered grid arrangement. This LES resolution is considered sufficiently accurate as in a previous study of flow over a bump using the same numerical method reasonable results have been obtained from a slightly coarser resolution at a higher Reynolds number (Wu and Squires 1998). The high ratio of  $\Delta x/\Delta z$  is meant to capture the long structure of near wall streaks.

In the RANS calculations the inflow profiles are obtained from a separate flat-plate boundary layer calculation using the same turbulence model. The Reynolds number of the flat plate flow ranges from 5000 at its inflow to 15000 at its outflow boundary and the solution at Reynolds number 10400 is extracted for the inflow profiles of the ramp simulation. A rescaling procedure is used to generate the time dependent inflow condition for LES (Lund *et al.* 1998). The time dependent solution is then extracted in the same way as in the RANS inflow generation. The inflow condition for both RANS and LES satisfies the universal log law. We also check the effect of upper boundary condition. From a computation using no-slip conditions along the upper wall, we confirm that there is no significant interference from the upper boundary in that no separation occur due to the adverse pressure gradient.

In addition, we compare the effect of Reynolds number on the solution with the theoretical prediction. The results of  $Re = 10400$  are compared to those of  $Re = 60000$ . The higher Reynolds number enhances the peak in the wall pressure, as shown in Figure 5, but suppress the peak in the shear stress and integral quantities, as illustrated by the skin friction in Figure 6 and the shape factor in Figure 7. The high Reynolds number skin friction prior to separation and in the recovery region is lower than that from the low Reynolds number case, in accordance with the case of zero pressure gradient. In theory, assuming that the streamwise velocity at the inlet has a  $1/7$  power-law profile, the skin friction at Reynolds number 10400 and 60000 (equivalent to  $Re_\theta = 1320$  and 7641) are  $4.24 \times 10^{-3}$  and  $2.73 \times 10^{-3}$ , respectively (Schlichting 1979, Equation 21.12). Our result produces the corresponding values of  $4.26 \times 10^{-3}$  and  $2.75 \times 10^{-3}$ , respectively. The level of the skin friction

after reattachment is much lower than the value on the flat plate boundary layer at the same  $Re_\theta$ . The local skin friction,  $c_f = 2\tau_w/(\rho U_e(x)^2)$ , after reattachment, however, is in fair agreement with the corresponding canonical value. Here,  $U_e(x)$  is the edge velocity as function of the streamwise coordinate, computed from the corresponding wall pressure coefficient. The inlet shape factor of the low Reynolds number case is about 1.4. The theoretical shape factor for the 1/7 power profile is about 1.286, which is closely mimicked by the inlet shape factor of the high Reynolds number case. The sharp peak in the shape factor is due to the sharp corner of the ramp. The results shown for this Reynolds number effect used the V2F model. Similar results are obtained using the other turbulence models.

## 4 Results

### 4.1 Mean and Integral Quantities

In this section we compare the results from the RANS cases, SA, V2F and MV2F, with those from potential flow and LES. Unlike in a backward facing step or in flow separation under APG or via blowing and suction, the pressure distribution in the present study is complicated by the existence of a strong favorable gradient due to the convex curvature of the ramp followed by an even stronger adverse pressure gradient due to the ramp corner stagnation (Figure 8). The separation is indicated by a small plateau in the neighborhood of the ramp corner ( $x/L_r=1$ , with  $L_r$  being the ramp length). The potential flow produces higher extrema in the wall pressure distribution due to the absence of viscous effects. As the region of non-rotational flow in the RANS and LES are smaller than in the potential flow, the viscous flow produces a lower wall pressure than the potential flow downstream of the ramp.

Figure 10 shows that following the flow acceleration the skin friction quickly decreases towards separation with the LES prediction being reaching zero prior to the RANS results. This rate of reduction in the wall stress from the LES, however, slows prior to reaching, resulting in about the same prediction in the separation position as in the RANS results. The slower approach in  $C_f$  towards zero in the LES is due to the intermittency in the separation location, which is not captured by the RANS models. We discuss the instantaneous separation of LES in more detail below. The S-A model shows a slower recovery compared to V2F model. The MV2F result substantially overestimates the skin friction in the recovery region. The slow recovery of S-A in the skin friction is also observed by Menter (1996) in the backward facing step. The separation location from S-A is slightly downstream of that predicted by V2F. In contrast to the separation point, the reattachment point is more affected by the different turbulence models. The LES produces the reattachment the furthest upstream followed by subsequently S-A, V2F and MV2F predictions.

The above statistical features are consistent with the contours of the separation bubble shown in Figure 9. The bubble contour is given by the value of  $y(x)$  which satisfies,

$$\int_0^y u(x, s) ds = 0, \quad (39)$$

where  $u$  is the mean streamwise velocity. The size of the separation bubble from S-A is comparable

to that of the LES, whereas the V2F models produce excessive bubbles with MV2F's being the largest. This over-estimation of the bubble size in combination with the late reattachment by the V2F models may explain the slow recovery of these models, especially the modified version, as discussed below. The fact that the results up to separation including the separation location from the different models agrees quite well shows that the models can handle attached flow under varying pressure gradient. The deviation in the bubble size and the reattachment location on the other hand indicate that modeling separated flows remains a delicate task, at least for the models considered here.

The good agreement in the separation location between LES and the RANS models is quite surprising as the instantaneous separation from LES is very volatile and spreads over a band of separation buffeting. This is shown in Figure 11 where the position of zero skin friction of the flow averaged over the spanwise direction are plotted against a time measure. The solid line represents the most upstream separation location and the dashed line the most downstream before the skin friction reaches its minimum value. Between these two lines there are small separation regions as illustrated by the streamwise development of the skin friction over the spanwise direction, but not in time (Figure 12). This region fluctuates strongly in time and the time-averaging results in the reduced rate in approach to zero in the skin friction, as shown in Figure 10. Unlike the separation location, the reattachment location shown in Figure 11 migrates in a less chaotic manner with time. The dashdot line is the most upstream reattachment location after the skin friction reaches the minimum value whereas the dotted curve in the figure are the most downstream. The figure shows an interesting feature in that the reattachment location is most of the time formed by a single line with jumps upward from time to time. It appears that there is a fraction of the separated region which cannot follow these sudden movement upwards and this part reattaches later in time as represented by the dots in the figure. This shedding process, however, does not occur periodically. A similar instantaneous behavior of the separation and reattachment location is also observed by Na and Moin (1996) in their DNS of turbulent separation under blowing and suction, but these investigators do not report a multiple in the separation or reattachment positions.

As a consequence of having a larger bubble size, V2F and MV2F results produce larger shape factors beginning from the middle of the separation region. The shape factor from all the models, including the LES, nearly returns to its equilibrium value of about 1.4 (Figure 13). Note, however, that this feature does not imply that the flow is recovered. In fact, at a moderate Reynolds number as used in the present study the canonical shape factor still depends on the Reynolds number, decreasing with increasing  $Re_\theta$  in the streamwise direction. A better measure for the recovery is the Clauser parameter,

$$G = \sqrt{2/C_f} \frac{H-1}{H}. \quad (40)$$

In Figure 14 the Clauser parameter from all the models suggests that the flow after reattachment is still far from recovered. The values of the Clauser parameter in equilibrium turbulent boundary layers range from 5.9 (Clauser) to 6.8 (Cole) according to Castro and Epik (1998), whereas the present values in the vicinity of the outflow boundary range from 7.3 (S-A) to 8 (V2F and MV2F). Even if the local skin friction is used, the Clauser parameter ranges from 6.8 to 7.6 which are still high for the canonical boundary layer.

Figure 15 shows the development of the streamwise velocity profiles plotted in semi-logarithmic coordinates, taken from the LES mean flow. It shows a large perturbation in the separation region and the recovery process following reattachment. In the logarithmic layer the streamwise velocity following reattachment drops below the log-law, which is typical in reattaching flows. The profiles then gradually increase and approach the log-law. The comparison of this recovery process amongst the various models is shown in Figure 16. It shows that the streamwise velocity profiles have recovered the log layer at  $x/L_r = 5.2$ , except for the MV2F result. The recovery of MV2F is distinctly slower than the other cases, which is consistent with the larger separation bubble and later reattachment described previously. The scatter between different models in the wake region on the other hand persists further downstream to  $x/L_r = 6.5$ , indicative of the flow probably not yet being fully recovered. The higher value of the Clauser parameter than usual for an equilibrium boundary layer supports this suspicion. Given that the Clauser parameter is a function of integrals of the profile, this parameter covers the inner and outer region. The difference in the mean flow recovery rate between the inner and the outer region is also reported by Alving and Fernholz (1995).

Figure 17 shows the development of the streamwise velocity profiles beginning from the center of separation. As already indicated by the skin friction, the RANS models produce a stronger reverse flow than predicted in LES in the separated region. Analogous behavior is observed by Michelassi *et al.* (1996) in comparison of V2F with the experiment of Driver and Seegmiller (1985) in the backward-facing step. The profiles from the V2F predictions become positive further from the wall compared to S-A and LES results, which also explains the larger size of the separation bubble. Proceeding further downstream, S-A profiles follow LES predictions closely up to about  $y/\delta = 0.3$ , which covers the inner layer. In the outer region of the logarithmic layer, S-A profiles consistently over-predict those from the LES. A similar picture emerged in the work of Menter (1996) in the comparison of an APG-induced separation with the experimental data from Driver (1991). On the contrary, V2F profiles under-estimate the recovery of LES in the inner log layer but shows a good agreement in the outer log layer, in agreement with Michelassi *et al.* (1996). The log layer extends in this case from  $y/\delta = 0.1$  up to 1.5. The low Reynolds number case of Michelassi *et al.* (1996), however, yields a better collapse with experiment. The MV2F results underestimates the recovery throughout nearly the entire extent of the log layer. Apparent is the later reattachment of the V2F models also corresponding to delayed recovery.

The good agreement in the velocity profiles between S-A and LES in the region very close to the wall contradicts with the view based on the skin friction in which S-A recovers more slowly than V2F. This suggests a relatively weak correlation in the velocity profile and wall shear stress in the recovery region. Accuracy in the predicted wall shear stress depends on the ability of the model to adequately account for processes affecting the velocity gradient at the wall. The recovery process in the turbulence structure is represented by the turbulent fluctuating quantities, discussed in the next section.

## 4.2 Turbulence Quantities

Figure 18 shows the normal stress  $v^2$  from LES, V2F and MV2F calculations at several downstream stations. The value of  $v^2$  from the RANS models are lower than the normal fluctuations in the LES in the reattachment zone. Note that this comparison is not one-to-one in the sense that  $v^2$  is simply a velocity scale in the V2F closure. The quantity can be associated with the wall-normal fluctuations in a flat-plate boundary layer, but is otherwise a velocity scale used in the model to determine the eddy viscosity. Nevertheless, its evaluation against wall-normal fluctuating velocities in the LES is useful. Proceeding downstream from reattachment the normal stress decays and the peak is taken over by MV2F model. Downstream of  $x/L_r = 3$  the decrease of MV2F is much slower than the other two cases, yielding a consistently higher  $v^2$ . The decay process persists up to below the level upstream of separation near the wall, indicating a very slow recovery of the normal stress. In general, the fluctuations from LES decay more quickly with the increasing distance from the wall than the RANS results. The original V2F and the modified version MV2F agree well in the attached region upstream to the separation point. The separation, however, brings deviations between the two in the recovery region.

As in  $v^2$ , the predictions of  $u^2$  in Figure 19 shows some discrepancies between the various models, especially in the inner region. The data of the RANS cases are reduced by using Boussinesq approximation,

$$\frac{\overline{u_i u_j}}{k} - \frac{2}{3} \delta_{ij} = -\frac{\nu_t}{k} S_{ij}. \quad (41)$$

The deviation tends, however, to decrease proceeding further downstream from reattachment.

Figure 20 shows the peak distribution of the Reynolds stress  $u'v'$  from LES, SA, V2F and MV2F in the streamwise direction. In the separation region the values of  $u'v'$  from the RANS models under-predict that from LES. The Reynolds shear stress drops directly after reattachment. The same behavior is observed in BFS flow (Kim *et al.* 1980, Le *et al.* 1997) but not in separated flows induced by APG (Driver 1991, Alving and Fernholz 1996, Na and Moin 1998) where the Reynolds shear stress levels remain high after reattachment before they begin to decay. This implies that the different behavior of the shear stress following reattachment between BFS and APG flows is primarily caused by the difference in geometry as opposed to the unsteadiness of the separation location.

The Reynolds shear stress from the various models are close to each other in the region upstream of separation as illustrated by the data at  $x/L_r = -3$  in Figure 21. Beginning at  $x/L_r = 3.97$  the Reynolds shear stress from the RANS cases in general over-estimates that from the LES. Consistent with the picture of the normal stresses,  $u^2$  and  $v^2$ , the shear stress from MV2F is always higher than V2F in the inner region with that of V2F closer to LES predictions. The Reynolds stress from the S-A model is close to V2F and LES in the inner layer but over-estimates them in the outer layer. The Reynolds stress in S-A is calculated using the strain rate tensor,  $S_{ij}$  and Boussinesq approximation shown above.

Despite the scatter among different models, they show a common behavior. The peak of the Reynolds stresses reaches its maximum in the separation region. In the course through the separation region the maxima move further away from the wall, which is clearly seen from the data just

downstream of the reattachment point. At the same time the stresses grow outward. Proceeding further in the streamwise direction, the maxima of the Reynolds stresses decrease gradually up to a lower value than prior to separation and tend to flatten. This flattening of the relaxing Reynolds stresses is also observed by other workers, e.g., Alving and Fernholz (1996), among others. At the reattachment region the stresses  $u^2$  and  $u'v'$  very close to the wall drop to a lower level than before separation. This at least can be seen clearly from the LES result. Further downstream from reattachment the flow very close to the wall flow begins to regain its stress level compared to the level before separation. This can be seen from the LES prediction of  $u^2$  which shows the formation of a sharp peak close to the wall. This process takes place rather slowly in that even in the most downstream location it is still far from recovered. In contrast to  $u^2$  and  $u'v'$ , the effect of the separation on  $v^2$  is apparently more permanent. The stress level still subsides across the shear layer. The recovery, which is shown to begin from the wall region by the other components of Reynolds stresses, has not yet appeared in this quantity.

Figure 22 shows the streamwise development of the peak of the turbulent kinetic energy from LES, V2F and MV2F model predictions. The kinetic energy is rescaled by its maximum value at the inflow boundary. The kinetic energy from LES increases the most rapidly in the separated flow region, followed by MV2F and V2F subsequently. Similar to the normal component of the Reynolds stress, the increase of the kinetic energy after separation is more rapid than its decrease after reattachment. Again, V2F and MV2F agree with each other upstream of the separation but respond differently to the separation. As in the predictions of the Reynolds stresses, the peak of the turbulence kinetic energy from V2F moves closer to that of LES than MV2F in the recovery region. As will be shown next, the decreasing peak after reattachment is located in the middle of the shear layer. The peak is then taken over by the flow adjacent to the wall during the re-development process further downstream.

Wall-normal profiles of the turbulent kinetic energy at several streamwise stations is shown in Figure 23. Although the maximum in the kinetic energy from the RANS cases, especially from MV2F case, is generally higher than that from LES, the kinetic energy levels become zero at about the same wall-normal location. The larger separation bubble predicted by the V2F models apparently does not result in the expansion of turbulence kinetic energy towards the outer region. The recovery process observed in the turbulent stresses is again seen in the kinetic energy. The elevated peak of the turbulence kinetic energy through the separation region moves away from the wall. Proceeding further downstream, the peak decreases rapidly up to below the level prior to flow separation and forms a plateau at the same time. A sharp peak gradually appears at the vicinity of the wall indicating that the region of energetic turbulent motions is beginning from the wall. The fall of the Reynolds stresses and the turbulence kinetic energy in the recovery region to the magnitude lower than in the zero pressure gradient case indicates that the recovery process of the turbulence quantities is not monotonic. A rebound process, albeit slowly evolving, will consequently follow the decay process.

At the furthest downstream location the turbulence structures remain strongly distorted from its canonical found in equilibrium boundary layers. The turbulence structure is evidently still far from recovered. A longer extent for the recovery region is required to see how the recovery process from the wall further evolves and how the outer layer returns to its canonical form. The outer layer

turbulence structure induced by the separation seems to possess a considerably long timescale. Note that in canonical boundary layers the turbulence structure also grows along with the growth of  $Re_\theta$ . For the current configuration, the boundary layer thickness for a zero pressure gradient layer at the current outflow boundary would be about 2.6 times its thickness at the inflow. The turbulence structure normally vanishes at some distance outside the boundary layer edge. In the present case the turbulence quantities become zero slightly above  $y/\delta = 3$ . Therefore it is unlikely that the energetic outer layer turbulence will further decay to return its canonical form. More likely is that the recovery of the turbulence structure is initiated from the inner layer near the wall.

The possibility still exists that the outer layer feeds the regeneration of the inner layer. In this case, the outer layer would play the dominant role in the recovery process as suggested by Alving and Fernholz (1996) and Castro and Epik (1998). The production term of the turbulence budget, however, confirms the presumption on the role of the inner layer as shown in Figure 24 and Figure 25. The former shows the production of the turbulent kinetic energy and shear stress at several streamwise stations while the latter shows the production of the streamwise and normal components of the Reynolds stress, respectively. These production terms are given by

$$P(k) = -\overline{u'v'}(\partial\overline{U}/\partial y + \partial\overline{V}/\partial x) + (\overline{u^2} - \overline{v^2})\partial\overline{V}/\partial y \quad (42)$$

$$P(-u'v') = \overline{u^2}\partial\overline{V}/\partial x + \overline{v^2}\partial\overline{U}/\partial y \quad (43)$$

$$P(u^2) = 2(\overline{u^2}\partial\overline{V}/\partial y - \overline{u'v'})\partial\overline{U}/\partial y \quad (44)$$

$$P(v^2) = -2(\overline{v^2}\partial\overline{V}/\partial y + \overline{u'v'})\partial\overline{V}/\partial x. \quad (45)$$

Although small,  $\partial\overline{V}/\partial x$  is included for completeness. The data is taken from the LES predictions and considered to be representative as the same trend is produced by the V2F models. The production of turbulent kinetic energy and Reynolds shear stress before separation ( $x/L_r = -3$ ) is dominant in the near wall region. The peaks shift to the middle of the shear layer just downstream of reattachment. The magnitude of the peak, however, decays proceeding streamwise and the peak is taken over by the near wall region. The domination of the near wall production term is more profound further downstream. The production term of  $u^2$  is similar to that of the turbulence kinetic energy. This term for  $v^2$  generally does not play a significant role. Only in the separation region up to reattachment it is markedly large and the peak is located closer to the wall than in other turbulence quantities though it drops rapidly further downstream. The small production term explains the distinctly slow recovery of  $v^2$ . In summary, the overall result on the turbulence quantities indicates that the outer layer plays the dominant role only in the decay process, whereas in the rebound process this role is taken over by the inner layer. The rebound of the inner layer proceeds very slowly indicating that the dissipation also plays a significant role in this region.

## 5 Conclusion

The flow considered in this study is complicated by the subsequence of acceleration due to the convex curvature of the ramp and deceleration due to the ramp corner. This results in a favorable pressure gradient upstream of the separation point and downstream of the reattachment point. This complication, however, does not significantly change the general feature of the recovery process as

observed by other workers. The instantaneous separation trajectory, as shown by the LES results, fluctuates at a higher frequency and more irregularly than reattachment trajectory. In addition, there are multiple separation locations indicating the existence of intermittent reverse flow regions upstream of the main separation region. The reattachment trajectory is mostly formed by a single line. A multiple in the reattachment locations occurs only sporadically and over very short time intervals, indicating the existence of shedding events. Beginning from about four ramp lengths downstream of the ramp the streamwise velocity profile from all the models, except MV2F, collapses to the universal log-law. There remain the high value of the Clauser parameter, however, suggesting that the outer layer of the mean flow has not fully recovered.

The rate of the increase in turbulence fluctuations at the beginning of the separation region is higher than the rate of their decrease after reattachment. Although the mean flow in the log layer is recovered, the turbulence structure is far from recovered to canonical profiles as in equilibrium boundary layers. The development of the turbulence stresses and kinetic energy through the separation region is characterized by the increase of the peak until it reaches a maximum in the middle of the separation region and the shift of the peak away from the wall. At the same time the turbulence level decreases very close to the wall but strongly increases in the outer region. Through the recovery region the peak tends to flatten and the near wall structure starts to regain the levels prior to separation. The recovery process of the turbulence quantities is not monotonic, however, in that it is characterized by a rapid decay process followed by a slow rebound process. The outer layer is more dominant during the decay while the inner layer initiates the rebound. The commonly observed drop of the Reynolds shear stress directly after reattachment in the BFS is believed to be typical for geometry induced separation flows rather than for flows with a fixed separation location. In APG induced separation this Reynolds shear stress decay is delayed.

Regarding the performance of the RANS models, upstream of the separation all the turbulence models show a good agreement between each other as well as with LES. Through the separation region and further downstream, however, V2F and MV2F predictions exhibit discrepancies with those from V2F model being closer to the LES results. MV2F recovers much more slowly than the other models, which is partly caused by its later reattachment and larger bubble size. As far as the mean flow is concerned, S-A yields a generally better agreement with LES than the V2F models, which is evident from the result of the separation bubble geometry, the location of the reattachment point, the integral quantities, and the streamwise velocity profiles. The Reynolds shear stress from S-A, however, decays too slowly with increasing wall normal coordinate. A slower recovery directly after reattachment is observed in the skin friction of S-A compared to the other models, which seems to be typical for this closure. In spite of this slow recovery in  $C_f$ , the velocity profiles follow the corresponding relaxation from LES better than the V2F models, indicating that the overall recovery rate cannot be judged from the behavior of the skin friction alone. The slow recovery of mean velocity seems to be typical for the V2F models in high Reynolds number reattaching flows. All the models over-predict the backflow in the recovery region.

The Reynolds stresses and the turbulence kinetic energy from V2F show a good overall agreement with those from LES. The agreement is better proceeding further downstream in the recovery region. MV2F consistently over-estimates the turbulence quantities in the recovery region. The inner layer dynamics of the turbulence kinetic energy and the streamwise component of Reynolds

stress during the rebound process is, however, only slightly captured by the turbulence models.

## References

- [1] Adams, E.W. and Johnston, J.P. 1988 Flow structure in the near wall zone of a turbulent separated flow, *AIAA Journal* **26**, No. 8, 932-939.
- [2] Alving, A.E. and Fernholz, H.H. 1996 Turbulence measurements around a mild separation bubble and downstream of reattachment, *J. Fluids Mech.* **322**, 297-328.
- [3] Alving, A.E. and Fernholz, H.H. 1995 Mean velocity scaling in and around a mild, turbulent separation bubble, *Phys. Fluids* **7**, No. 8, 1956-1969.
- [4] Bradshaw, P. and Wong, F.Y.F. 1972 The reattachment and relaxation of a turbulent shear layer, *J. Fluid Mech.* **52**, 113-135.
- [5] Castro, I.P. and Epik, E. 1998 Boundary layer development after a separated region, *J. Fluid Mech.* **374**, 91-116.
- [6] Chorin, A.J. 1967 A numerical method for solving incompressible viscous flow problems, *J. Comp. Physics* **2**, 745-762.
- [7] Dengel, P. and Fernholz, H.H. 1990 An experimental investigation of an incompressible turbulent boundary layer in the vicinity of separation, *J. Fluid Mech.* **212**, 615-636.
- [8] Driver, D.M. 1991 Reynolds shear stress measurements in a separated boundary layer flow, *AIAA Paper* 91-1787.
- [9] Driver, D.M. and Seegmiller, H.L. 1985 Features of a reattaching turbulent shear layer in divergent channel flows, *AIAA Journal* **23**, No. 2, 163-171.
- [10] Durbin, P.A. 1991 Near wall turbulence closure modeling without dumping functions, *Theor. Comp. Fluid Dyn.* **3**, No. 1, 1-13.
- [11] Durbin, P.A. and Belcher, S. E. 1992 Scaling of adverse pressure gradient turbulent boundary layers, *J. Fluid Mech.* **238**, 699-722.
- [12] Durbin, P.A. 1995 Separated flow computations with  $k - \epsilon - v^2$  model, *AIAA Journal* **33**, 659-664.
- [13] Germano, M., Piomelli, U., Moin, P. and Cabot, W.H. 1991 A dynamic subgrid-scale eddy viscosity model, *Phys. Fluids A* **3**, No. 7, 1760-1765.
- [14] Ghosal, S. and Moin, P. 1995 The basic equations for the large eddy simulation of turbulent flows in complex geometry, *J. Comp. Phys.* **118**, No. 1, 24-37.

- [15] Iaccarino, G. and Durbin, P.A. 1996 Application of the  $k - \epsilon - v^2$  model to multi-component airfoils, Proceedings 1996 Summer Program, Center for Turbulence Research, 23-34.
- [16] Kim, J., Kline, S.J. and Johnston, J.P. 1980 Investigation of a reattaching turbulent shear layer: flow over a backward-facing step, *J. Fluid Eng.* **102**, 302-308.
- [17] Lien, S.F and Durbin, P.A. 1996 Non-linear  $k - e - v^2$  modeling with application to high-lift, Proceedings 1996 Summer Program, Center for Turbulence Research, 5-22.
- [18] Lilly, D.K. 1992 A proposed modification of the Germano subgrid scale closure method, *Phys. Fluids A* **4**, No. 3, 633-635.
- [19] Le, H., Moin, P. and Kim, J. 1997 Direct numerical simulation of turbulent flow over a backward facing step, *J. Fluid Mech.* **330**, 349-374.
- [20] Lund, T.S., Wu, X. and Squires, K.D. 1998 Generation of turbulent inflow data for spatially developing boundary layer simulations, *J. Comp. Phys.* **140**, 233-258.
- [21] Menter, F.R. 1996 A comparison of some recent eddy-viscosity turbulence models, *J. Fluid Eng.* **118**, 514-519.
- [22] Michelassi, P.A., Durbin, P.A. and Mansour, N.N. 1996 Prediction of the backflow and recovery regions in the backward facing step at various Reynolds numbers, Proceedings 1996 Summer Program, Center for Turbulence Research, 73-86.
- [23] Na, Y and Moin, P. 1998 Direct numerical simulation of a separated turbulent boundary layer, *J. Fluid Mech.* **374**, 379-405.
- [24] Perry, A.E. and Schofield, W.H. 1973 Mean velocity and shear stress distributions in turbulent boundary layers, *Pys. Fluids* **16**, 2068-2074.
- [25] Schlichting, H. 1979 *Boundary Layer Theory*, McGraw-Hill.
- [26] Simpson, R.L., Chew, Y.T. and Shivaprasad, B.G. 1981 The structure of a separating turbulent boundary layer, Parts 1 and 2, *J. Fluid Mech.* **113**, 23-73.
- [27] Simpson, R.L., Strickland, J.H. and Barr, P.W. 1977 Failures of a separating turbulent boundary layer in the vicinity of separation, *J. Fluid Mech.* **79**, 553-594.
- [28] Smits, A.J. and Wood, D.H. 1985 The response of turbulent boundary layers to sudden perturbations, *Ann. Rev. Fluid Mech.* **17**, 321-358.
- [29] Spalart, P.R. and Allmaras, S.R. 1994 A one equation turbulence model for aerodynamic flows, *La Recherche Aerospatiale*, No. 1, 5-21.
- [30] Stratford, B.S. 1959a The prediction of separation of turbulent boundary layer, *J. Fluid Mech.* **5**, 1-16.

- [31] Stratford, B.S. 1959b An experimental flow with zero skin friction throughout its region of pressure rise, *J. Fluid Mech.* **5**, 17-35.
- [32] Temam, R. 1979 *Navier-Stokes Equations. Theory and Numerical Analysis*, 2nd ed., North-Holland, Amsterdam.
- [33] Wu, X. and Squires, K.D. 1994 Towards large-eddy simulation of complex geometry turbulent boundary layer flows: extension of fractional step method to nonorthogonal curvilinear systems,
- [34] Wu, X. and Squires, K.D. 1998 Prediction of the high Reynolds number flow over a two dimensional bump, *AIAA Journal* **36**, No. 5, 798-808.
- [35] Yaglom, A. M. 1979 Similarity laws for constant pressure and pressure gradient turbulent wall flows, *Ann. Rev. Fluid Mech.* **11**, 505.

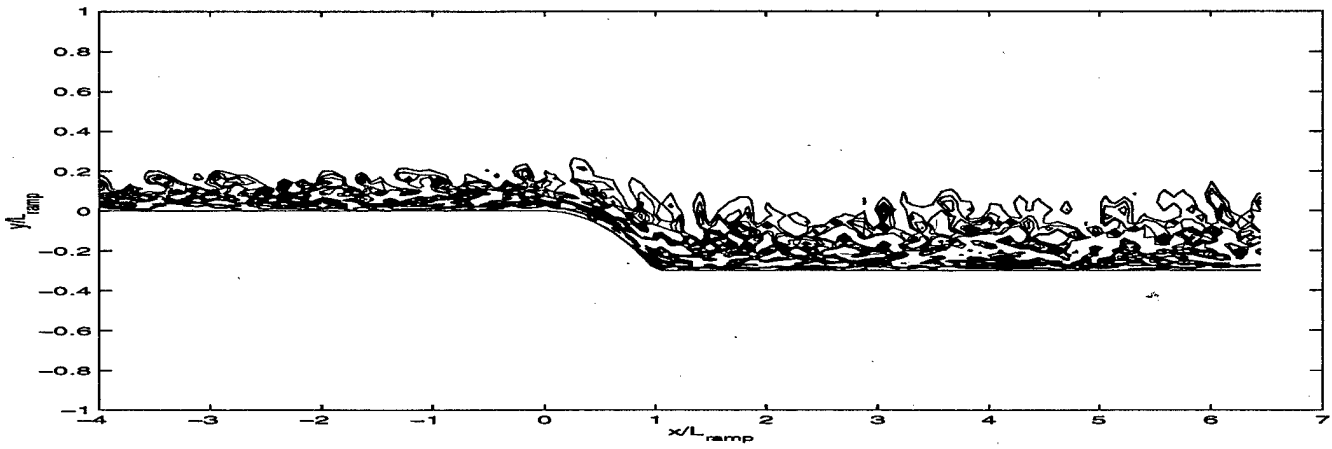


Figure 1: LES predictions of spanwise vorticity contours at the center plane.

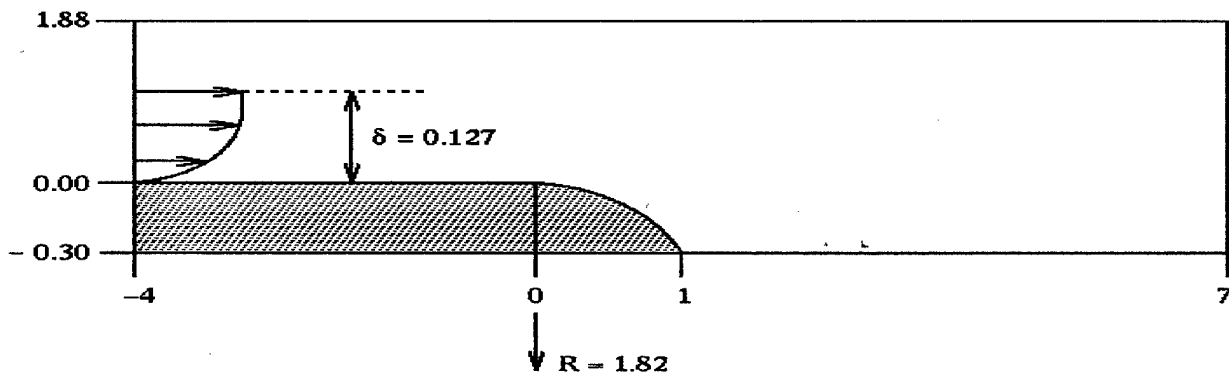


Figure 2: Ramp dimensions.

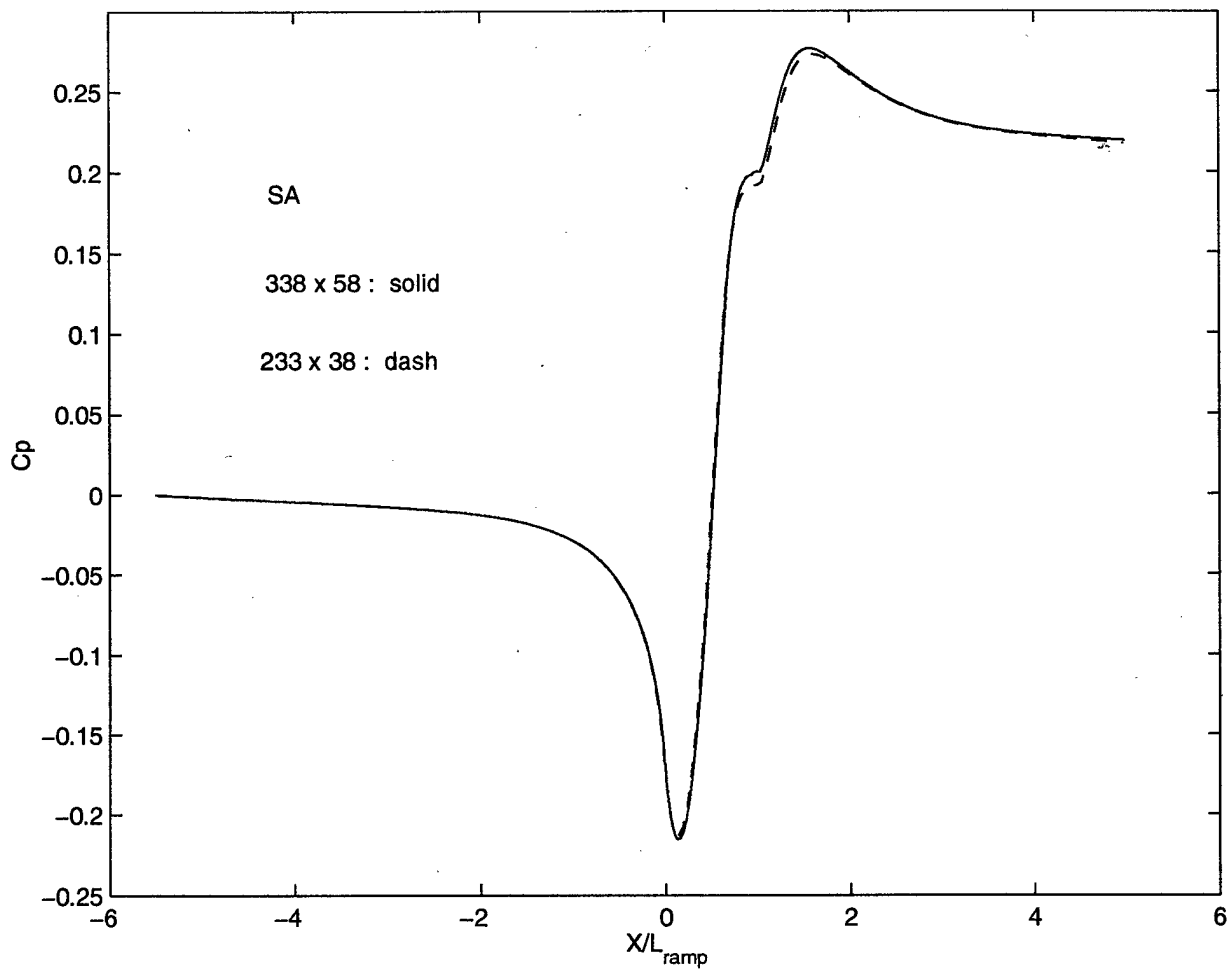


Figure 3: Effect of grid resolution on wall pressure coefficient predicted using S-A model.  $338 \times 58$  (solid) compared to  $233 \times 38$  (dash).

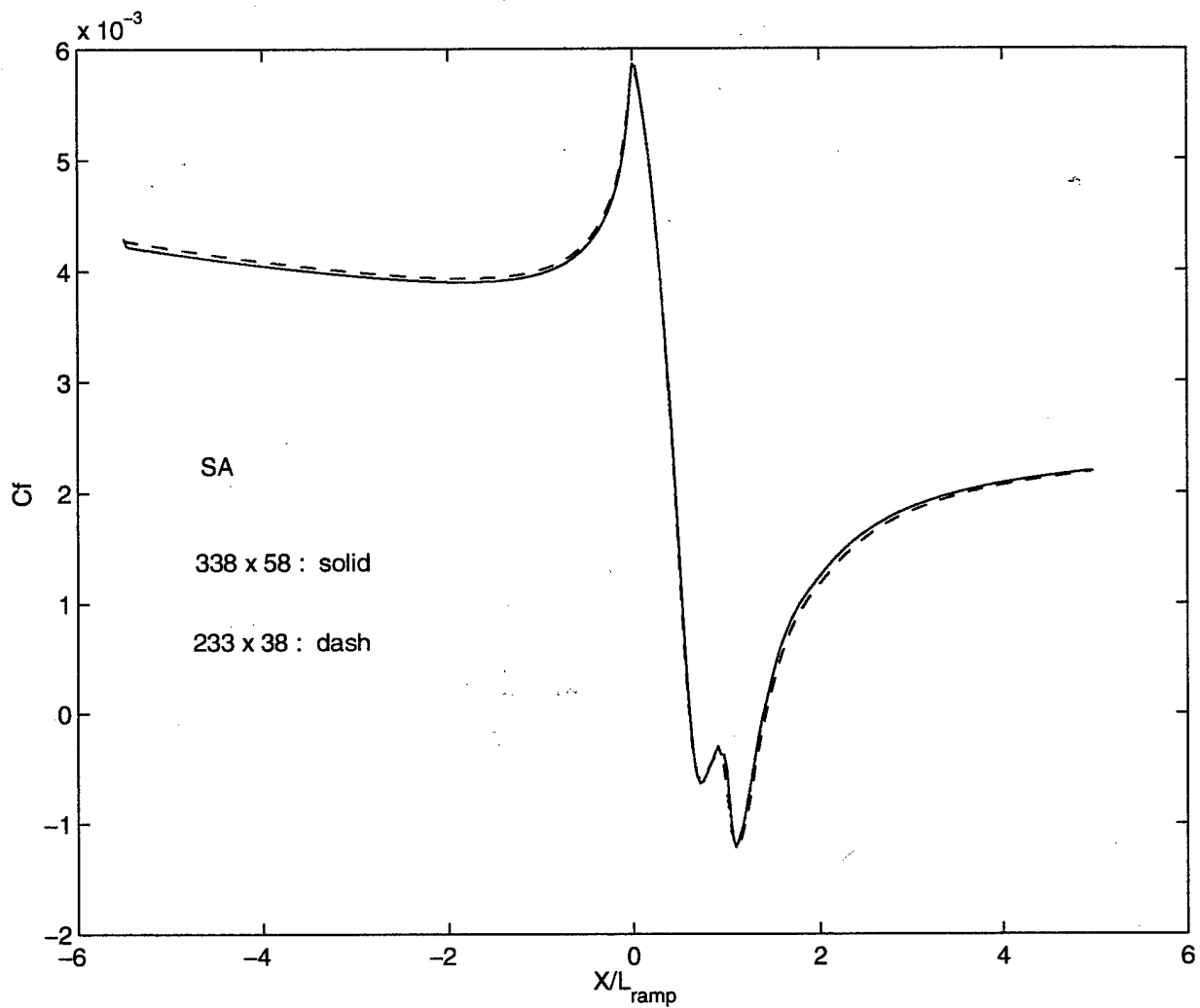


Figure 4: Effect of grid resolution on skin friction coefficient using S-A model.  $338 \times 58$  (solid) compared to  $233 \times 38$  (dash).

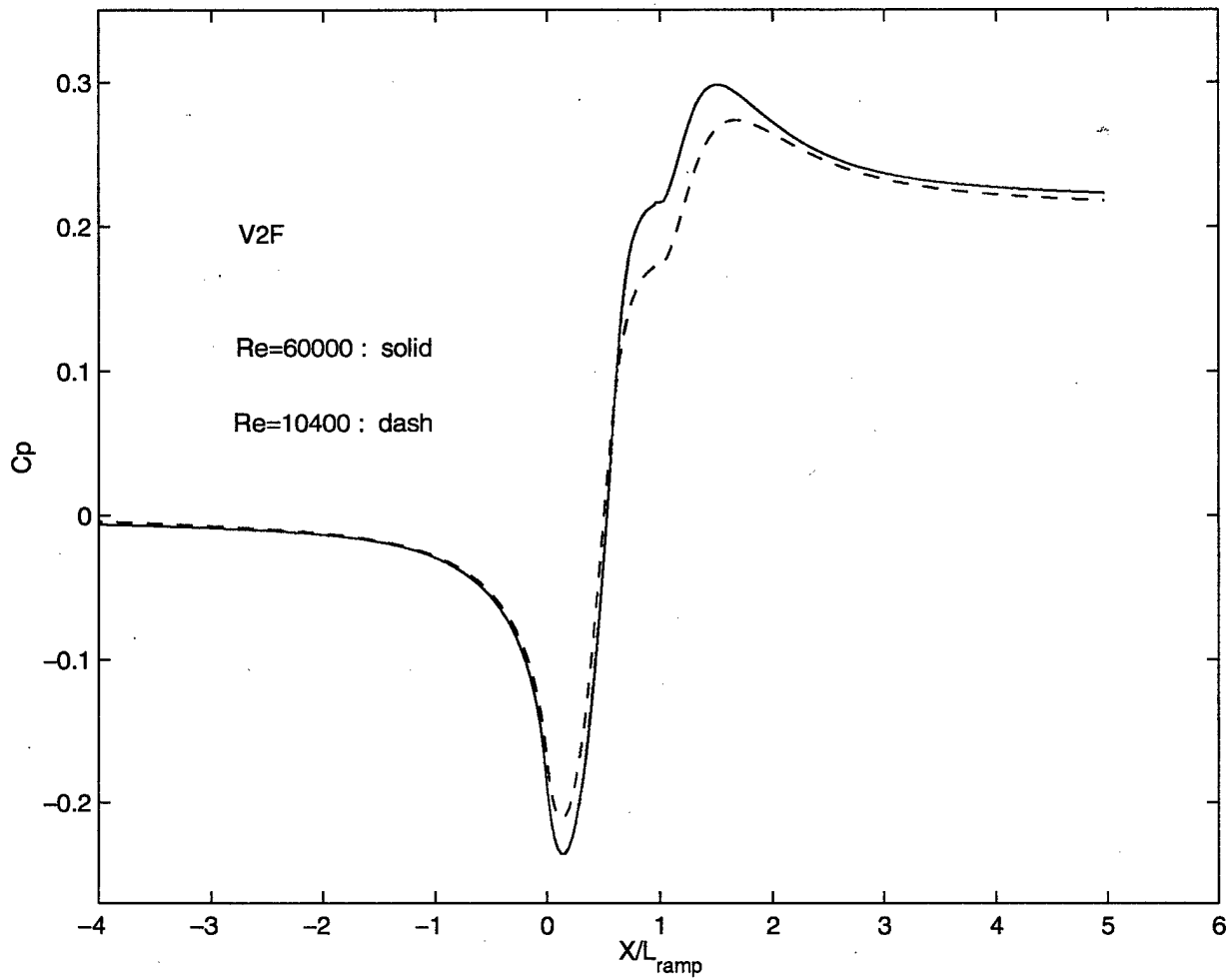


Figure 5: Wall pressure coefficient at Reynolds number 10400 (dash) and 60000 (solid).

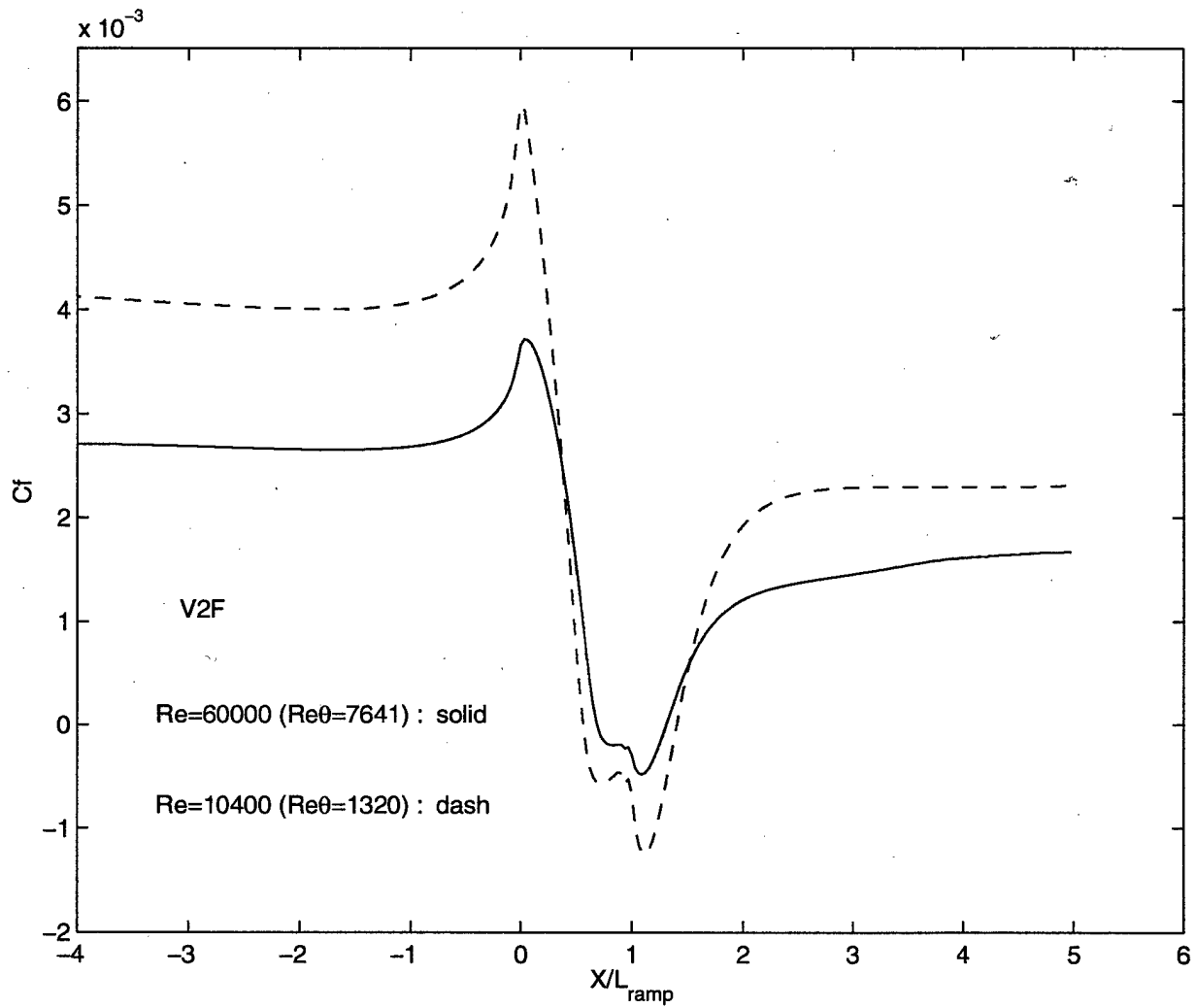


Figure 6: Skin friction coefficient using V2F model at Reynolds number 10400 (dash) and 60000 (solid).

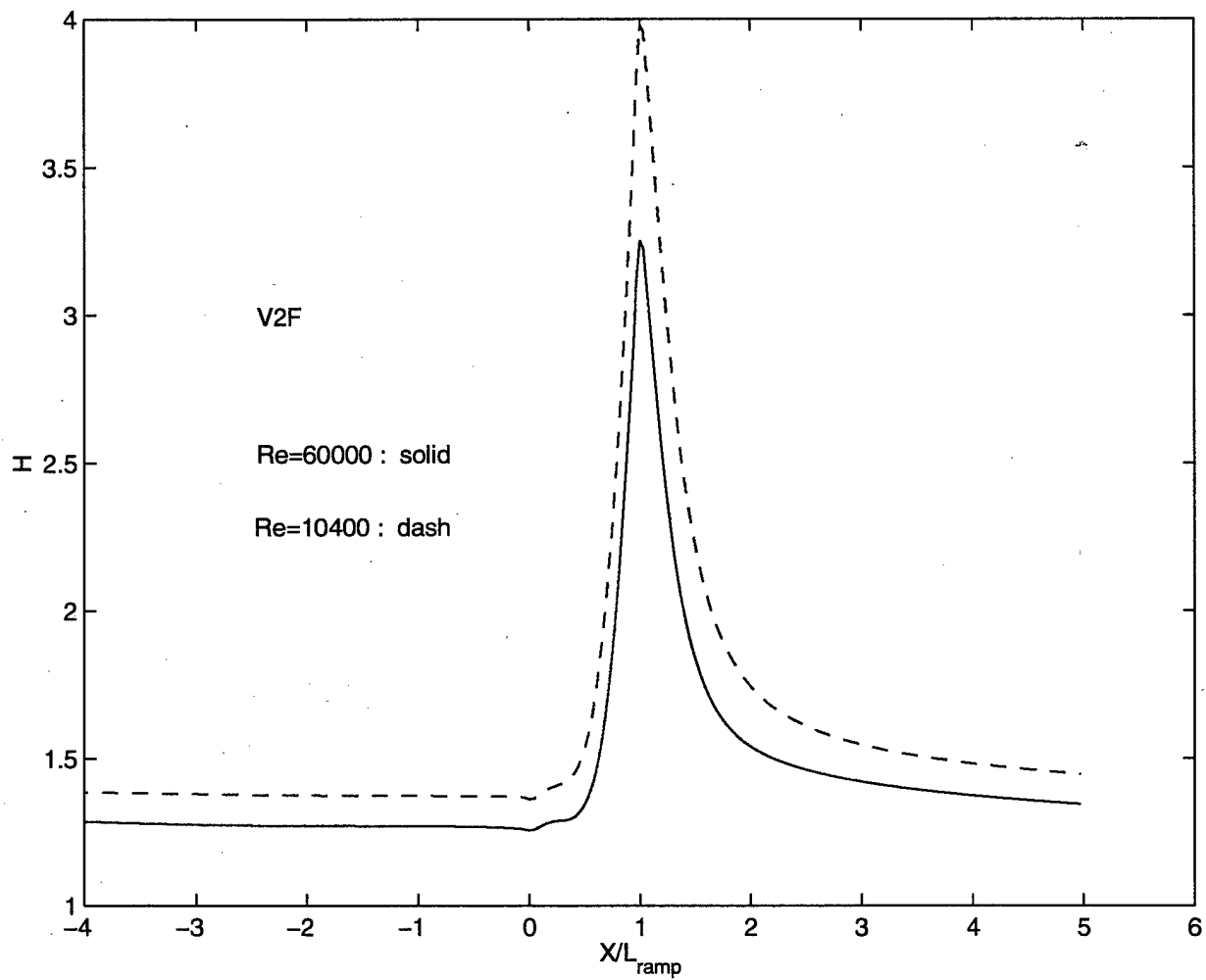


Figure 7: Shape factor using V2F model at Reynolds number 10400 (dash) and 60000 (solid).

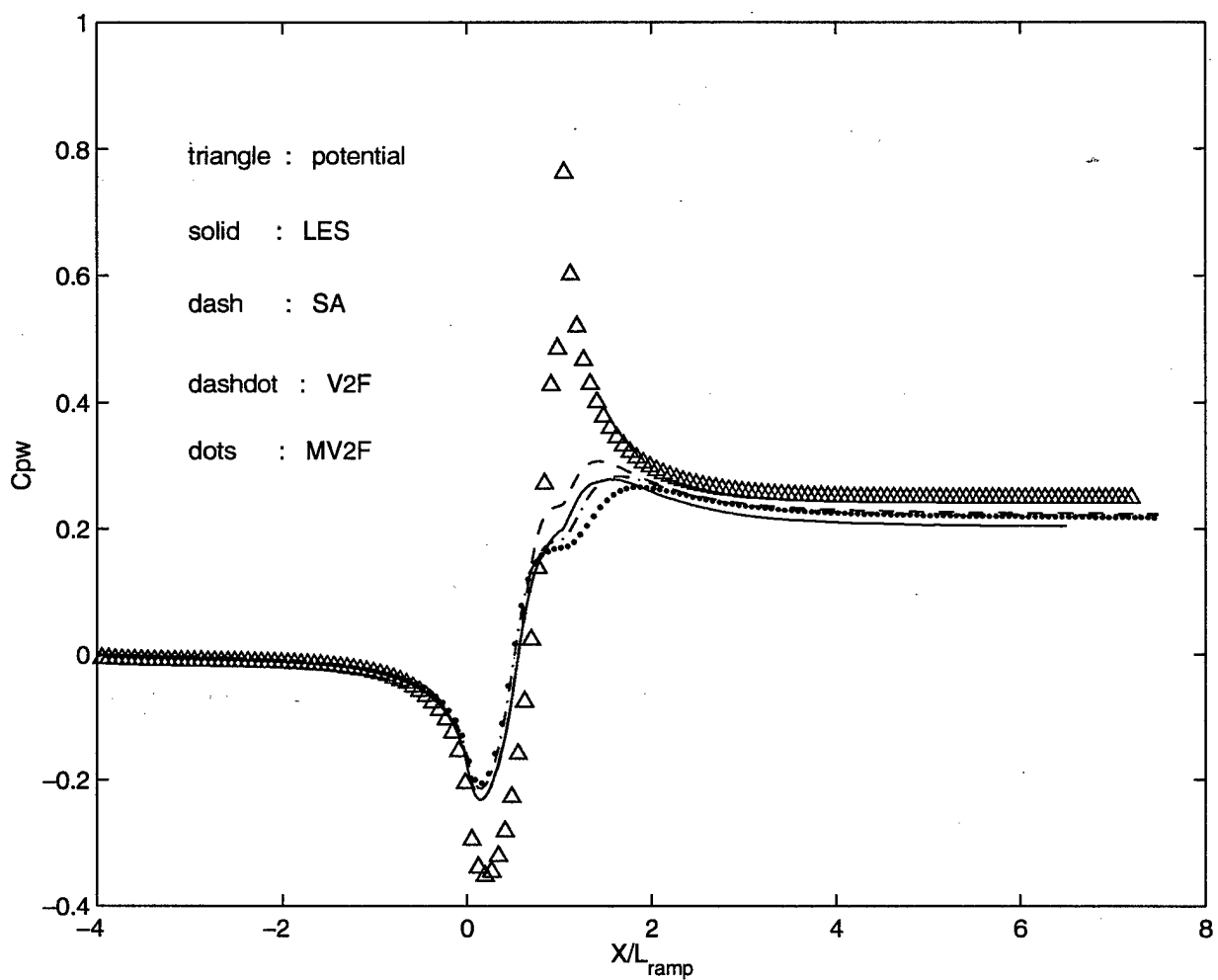


Figure 8: Wall pressure coefficient at Reynolds 10400; triangle: potential flow, solid: LES, dash: S-A, dashdot: V2F, dots: MV2F.

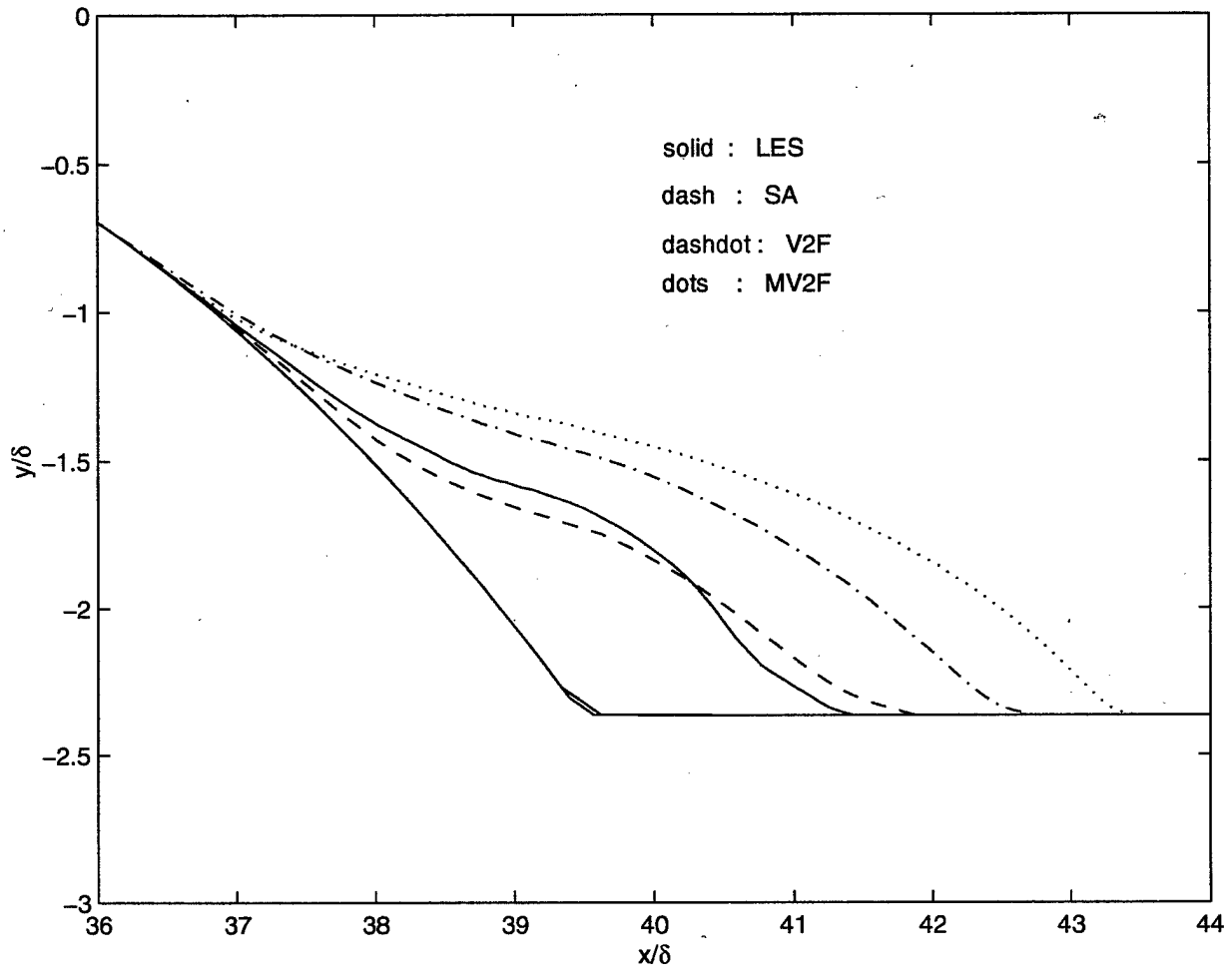


Figure 9: Contour of separation bubble; solid: LES, dash: S-A, dashdot: V2F, dots: MV2F.

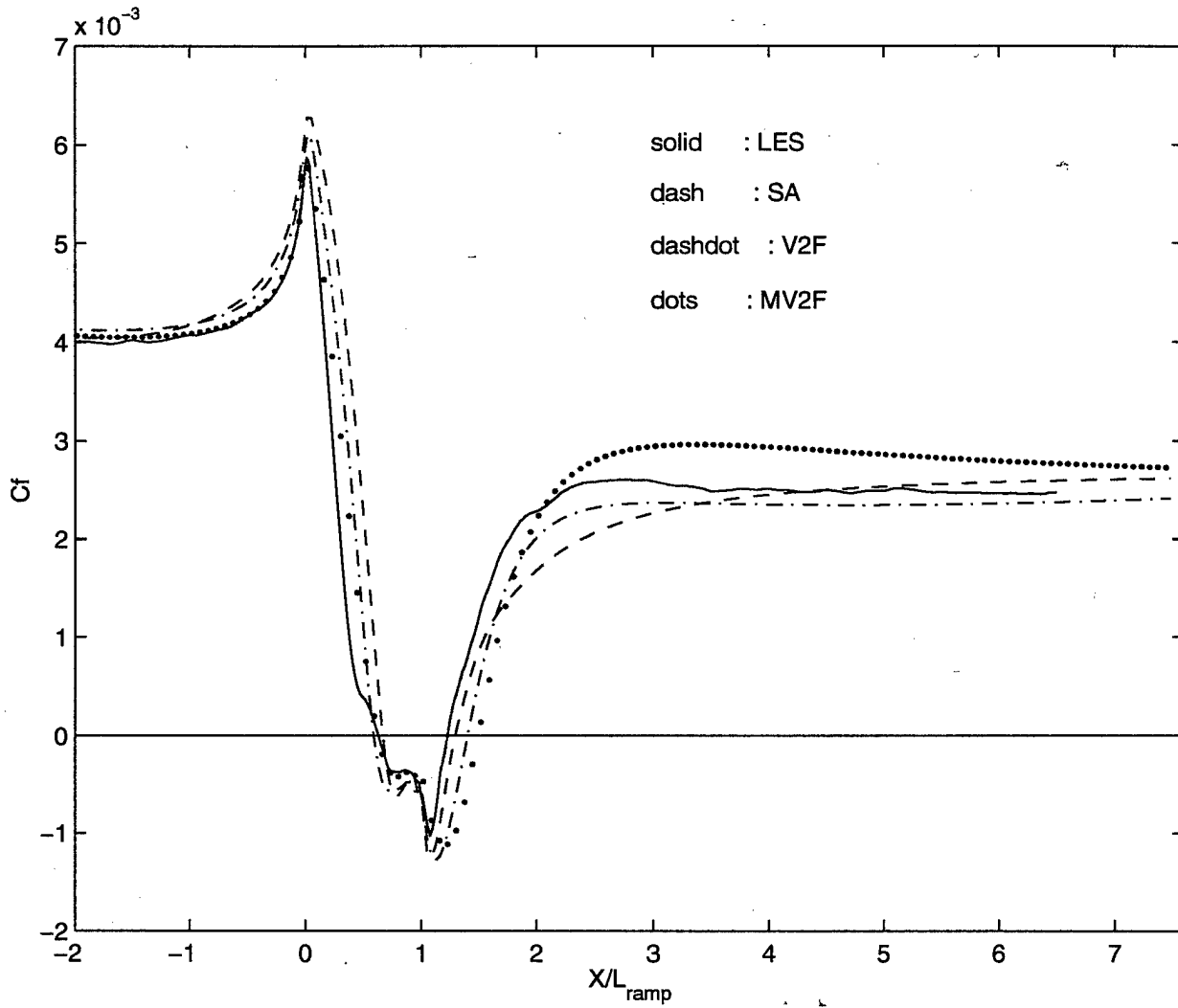


Figure 10: Skin friction coefficient; solid: LES, dash: S-A, dashdot: V2F, dots: MV2F.

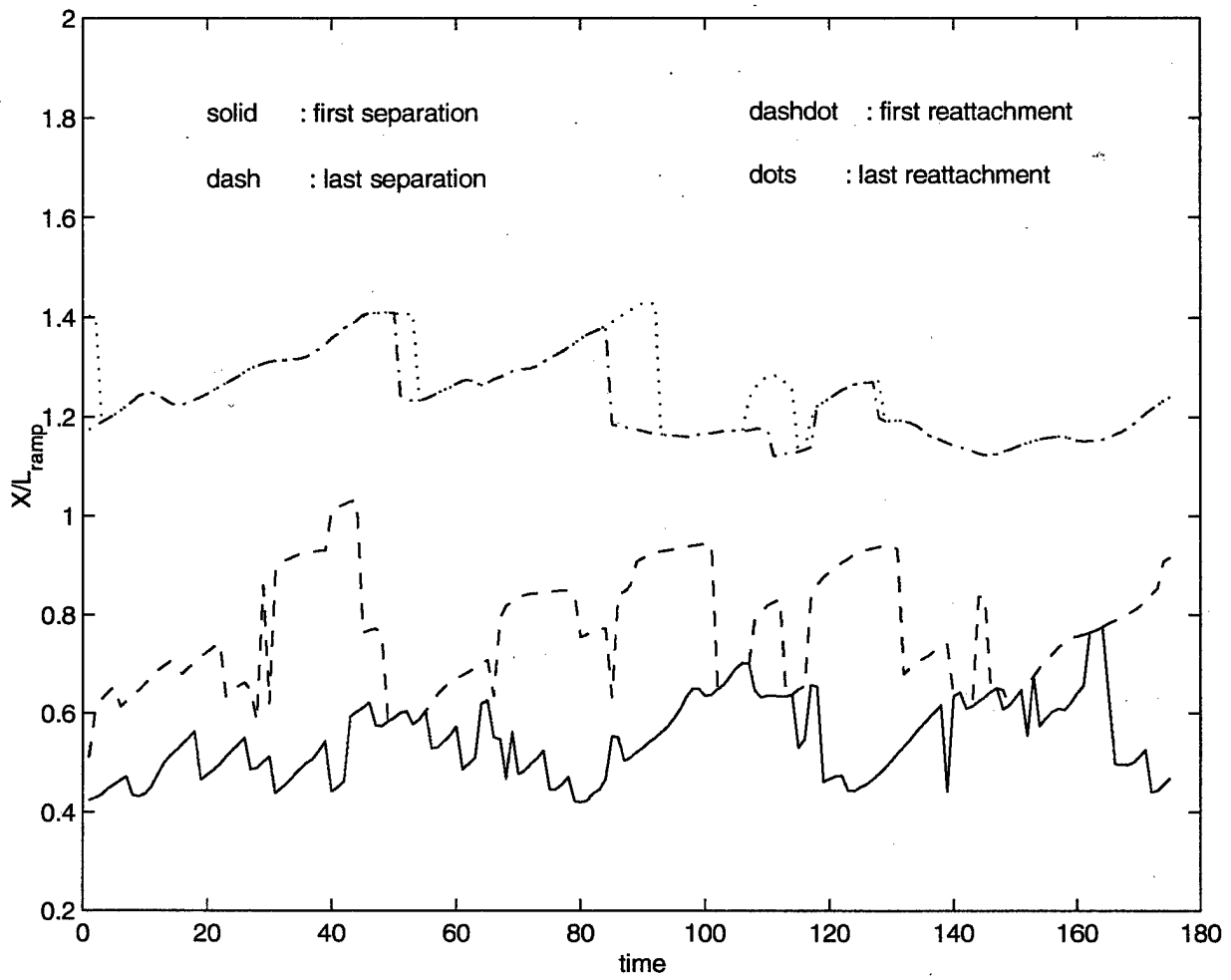


Figure 11: Migration of separation and reattachment point in time. solid: first separation, dash: last separation, dashdot: first reattachment, dots: last reattachment.

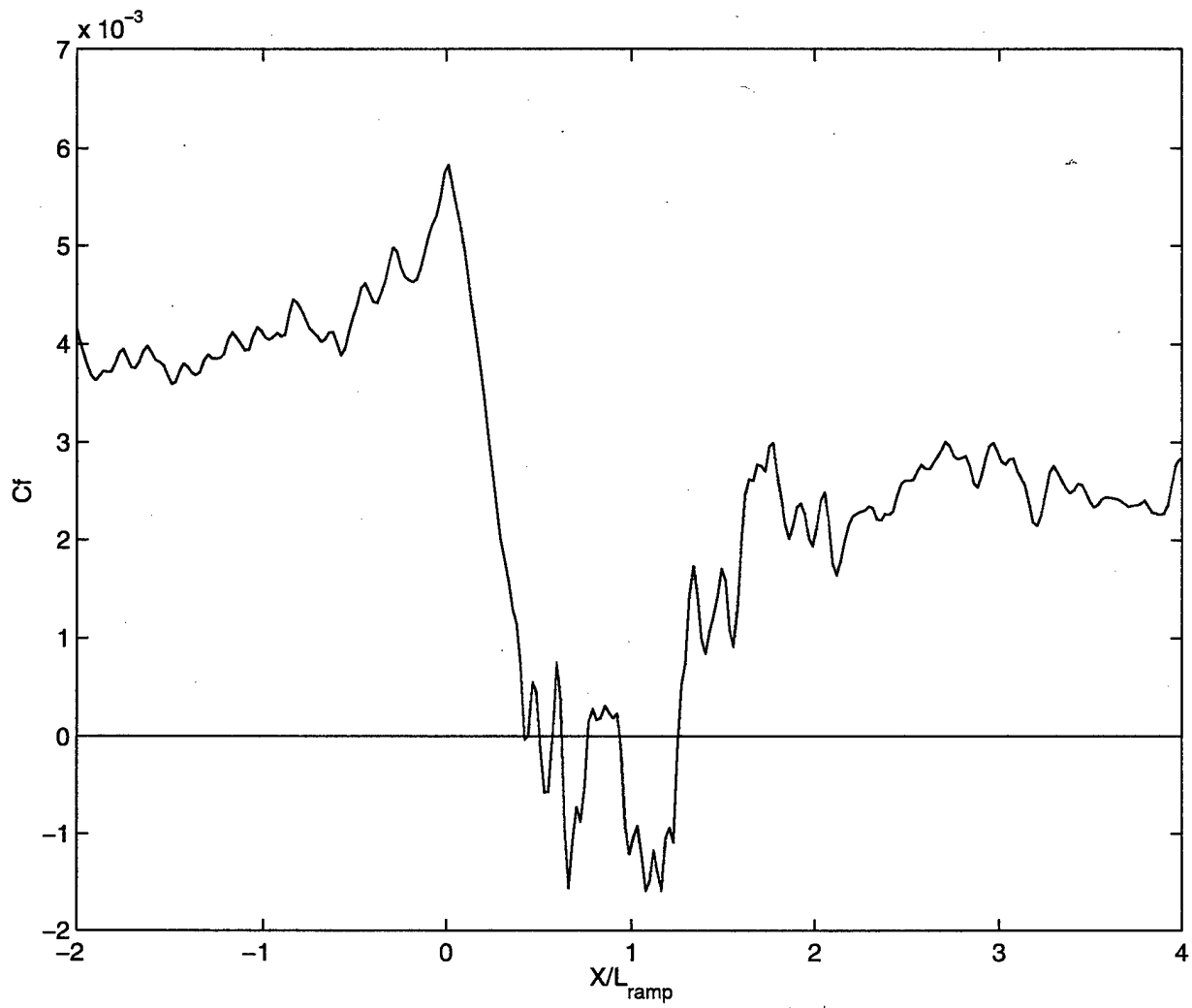


Figure 12: Skin friction of spanwise-averaged flow.

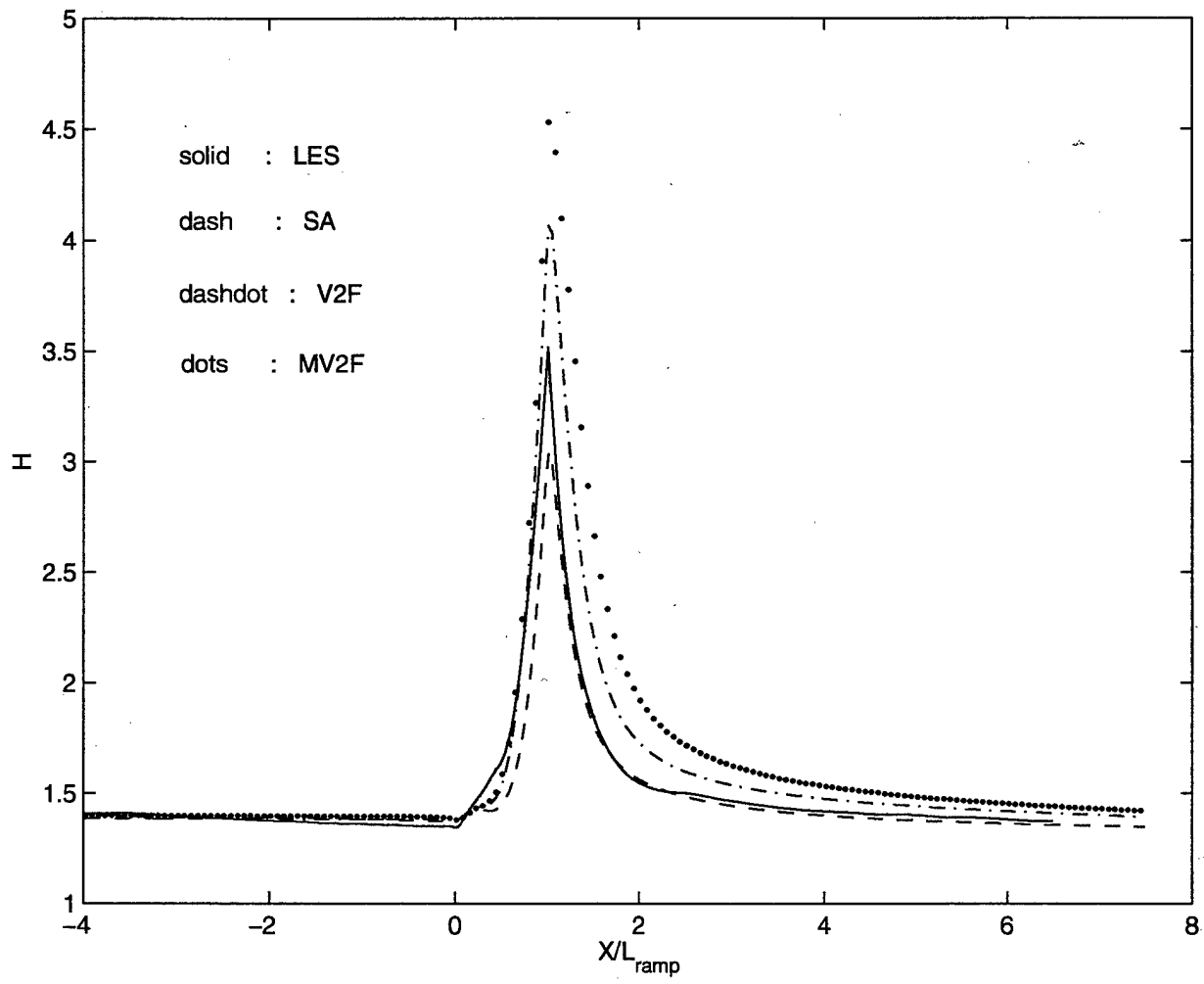


Figure 13: Shape factor; solid: LES, dash: S-A, dashdot: V2F, dots: MV2F.

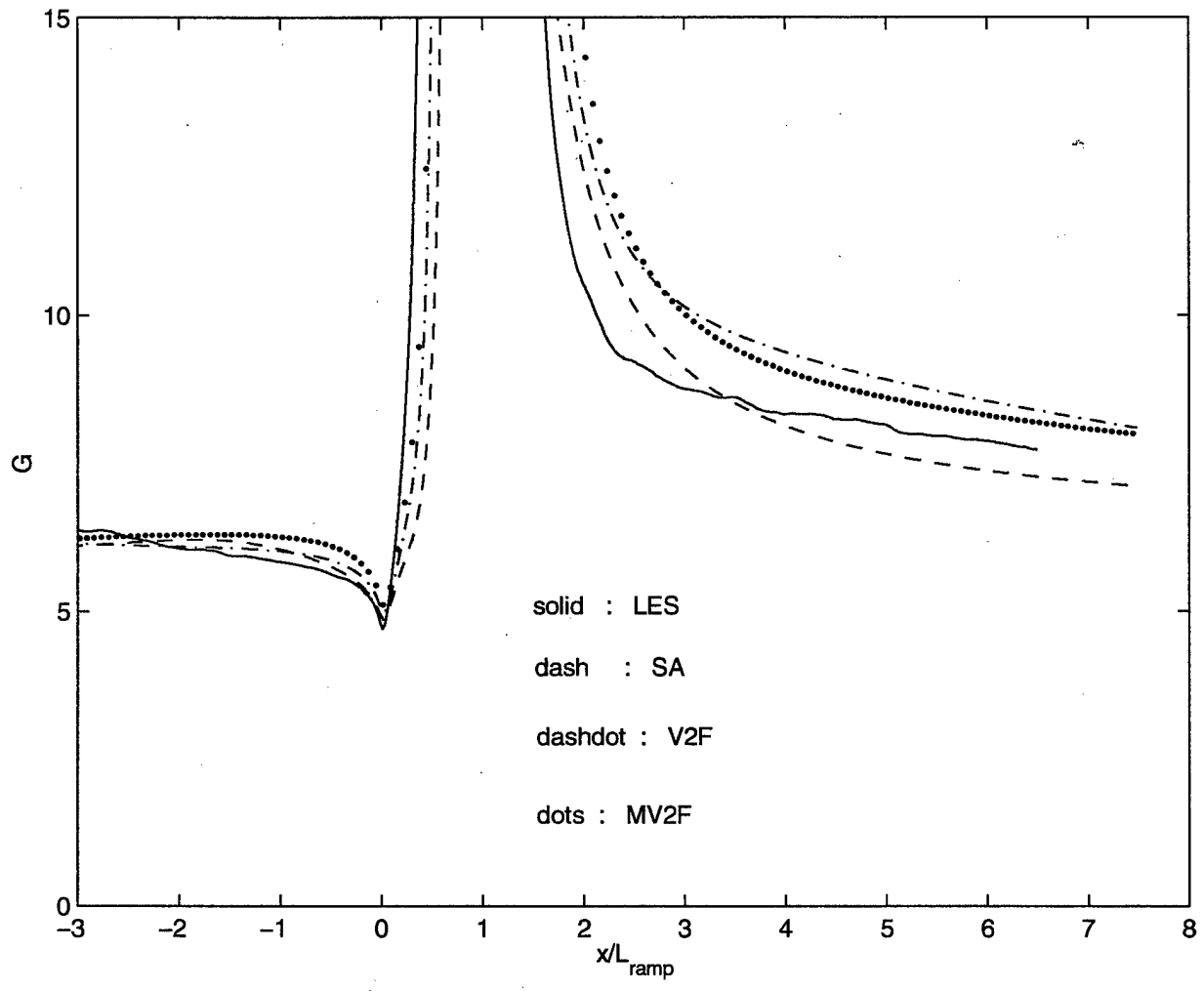


Figure 14: Clauser parameter; solid: LES, dash: S-A, dashdot: V2F, dots: MV2F.

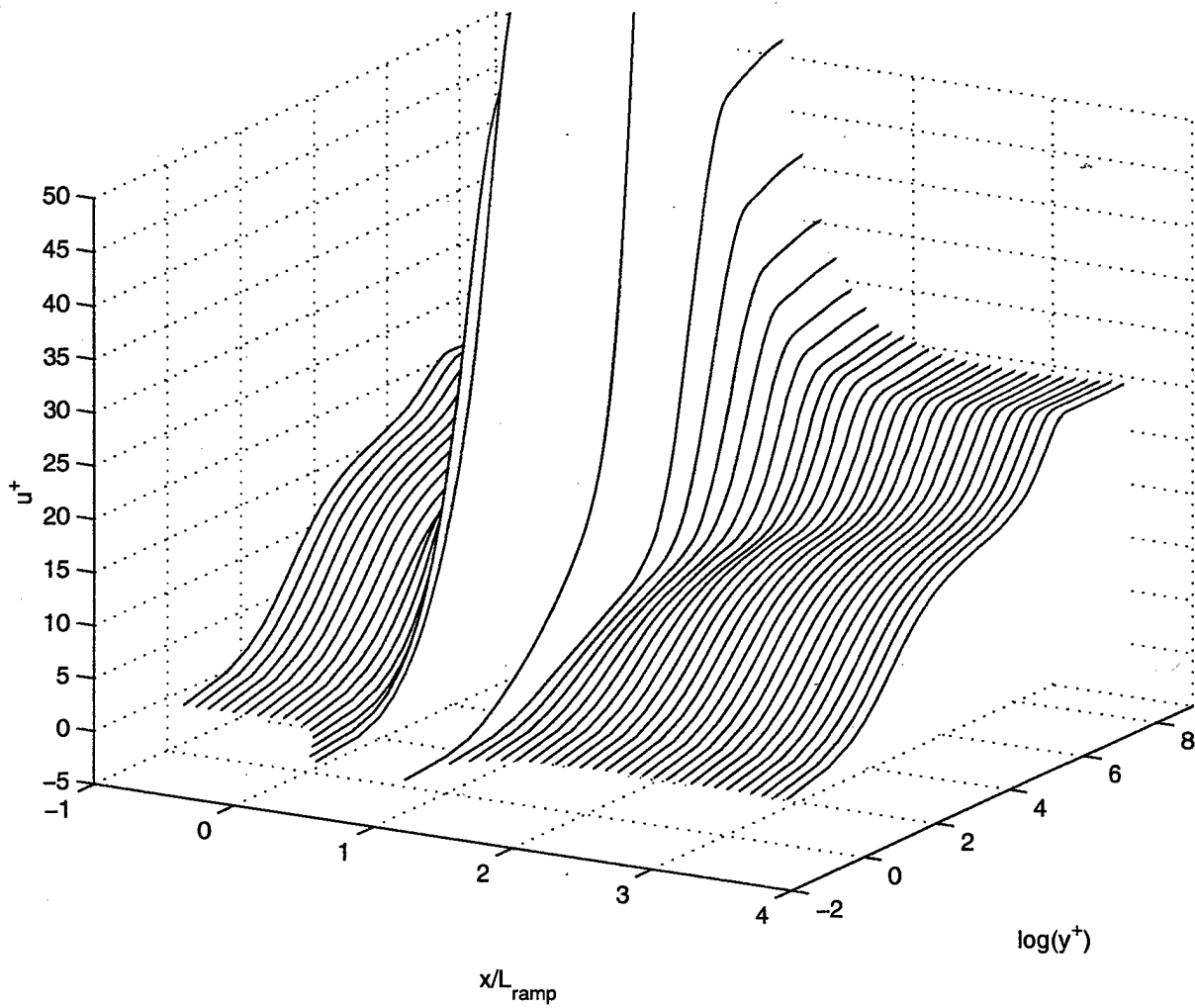


Figure 15: Development of the streamwise velocity log-profiles in the x-direction, taken from LES mean flow.

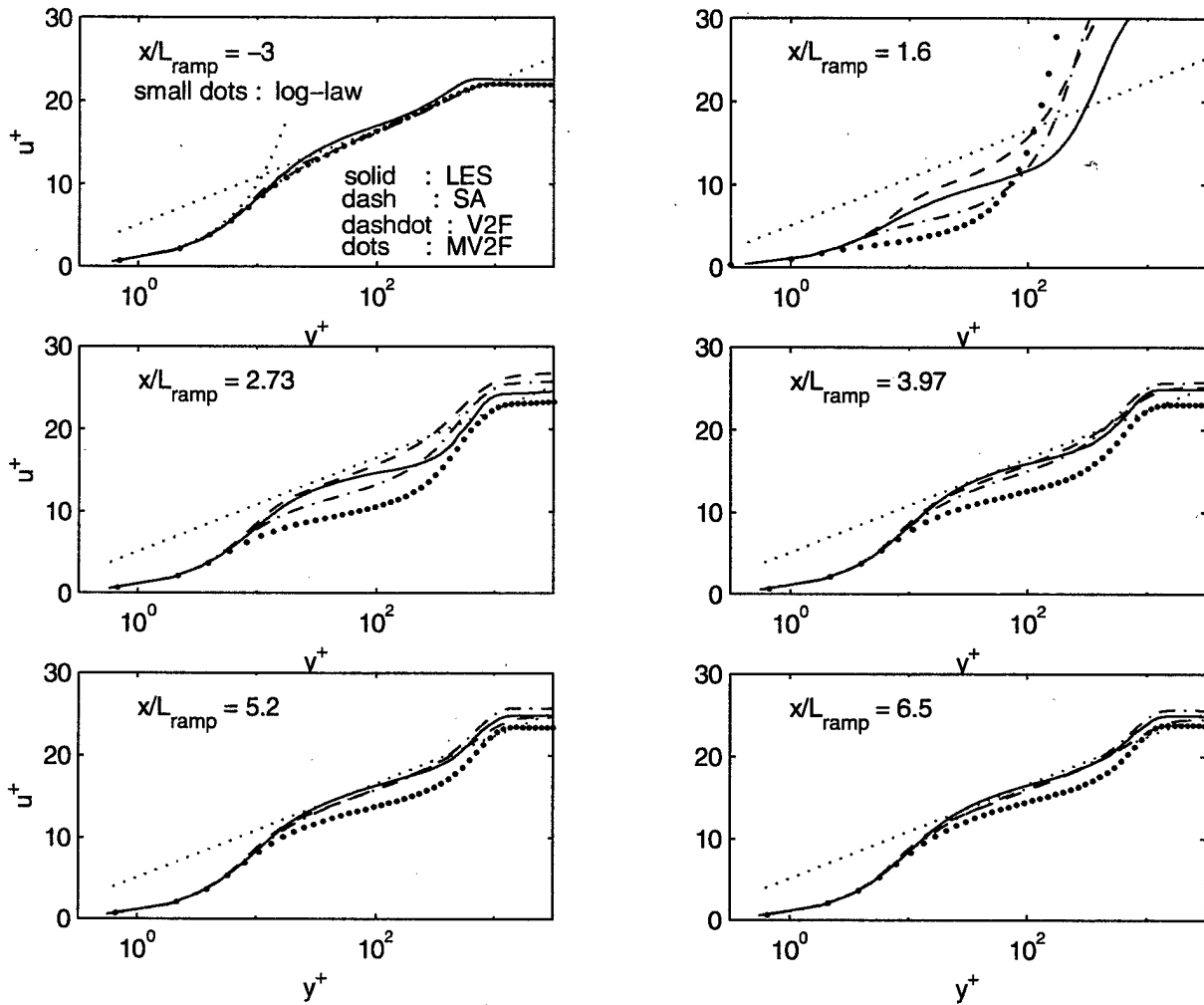


Figure 16: Streamwise velocity profiles at  $x/L_r = -3, 1.6, 2.73, 3.97, 5.2, 6.5$ ; solid: LES, dash: S-A, dashdot: V2F, dots: MV2F.

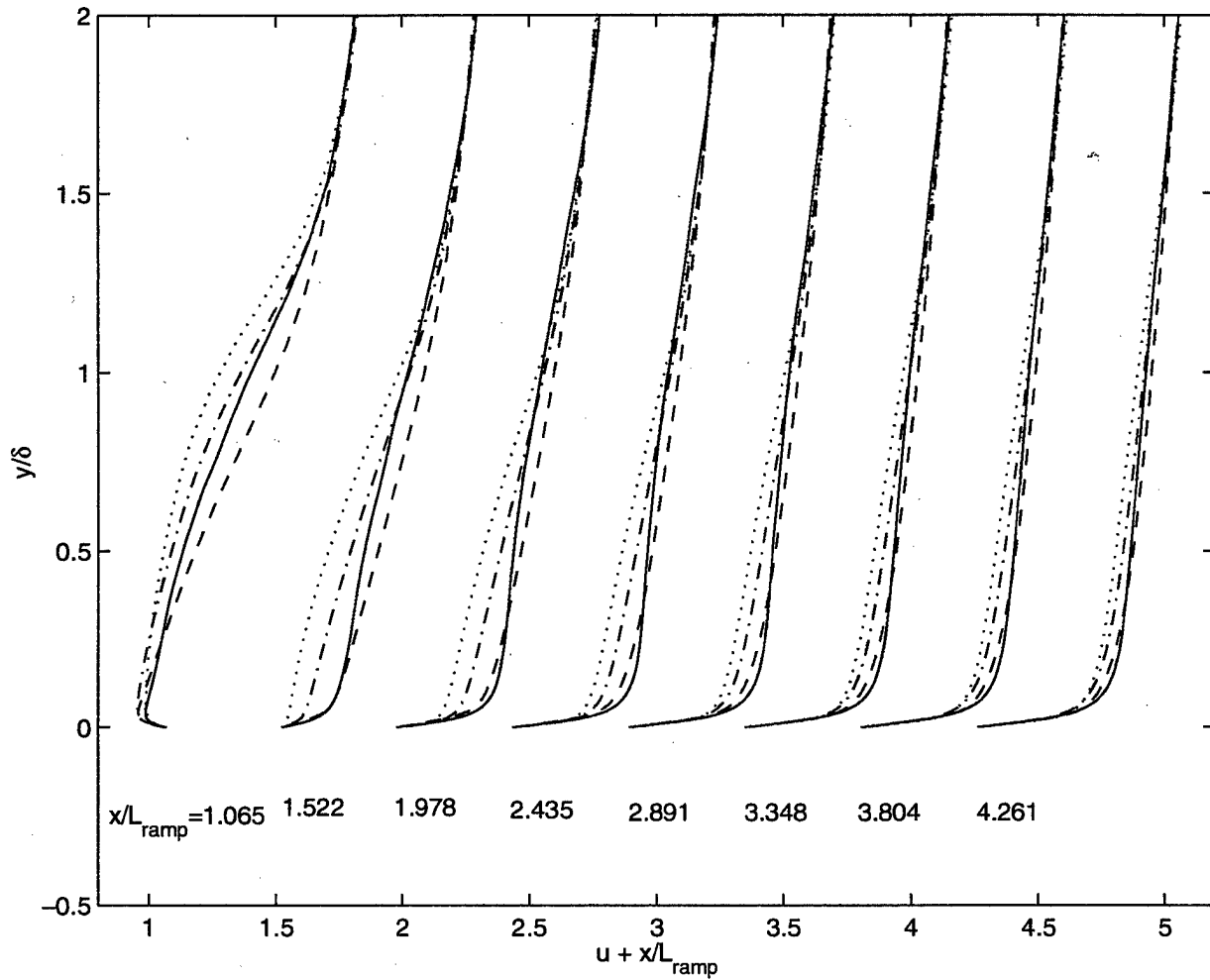


Figure 17: Streamwise velocity profiles at  $x/L_r = 1.07, 1.52, 1.98, 2.44, 2.89, 3.35, 3.80, 4.26$ ; solid: LES, dash: S-A, dashdot: V2F, dots: MV2F.

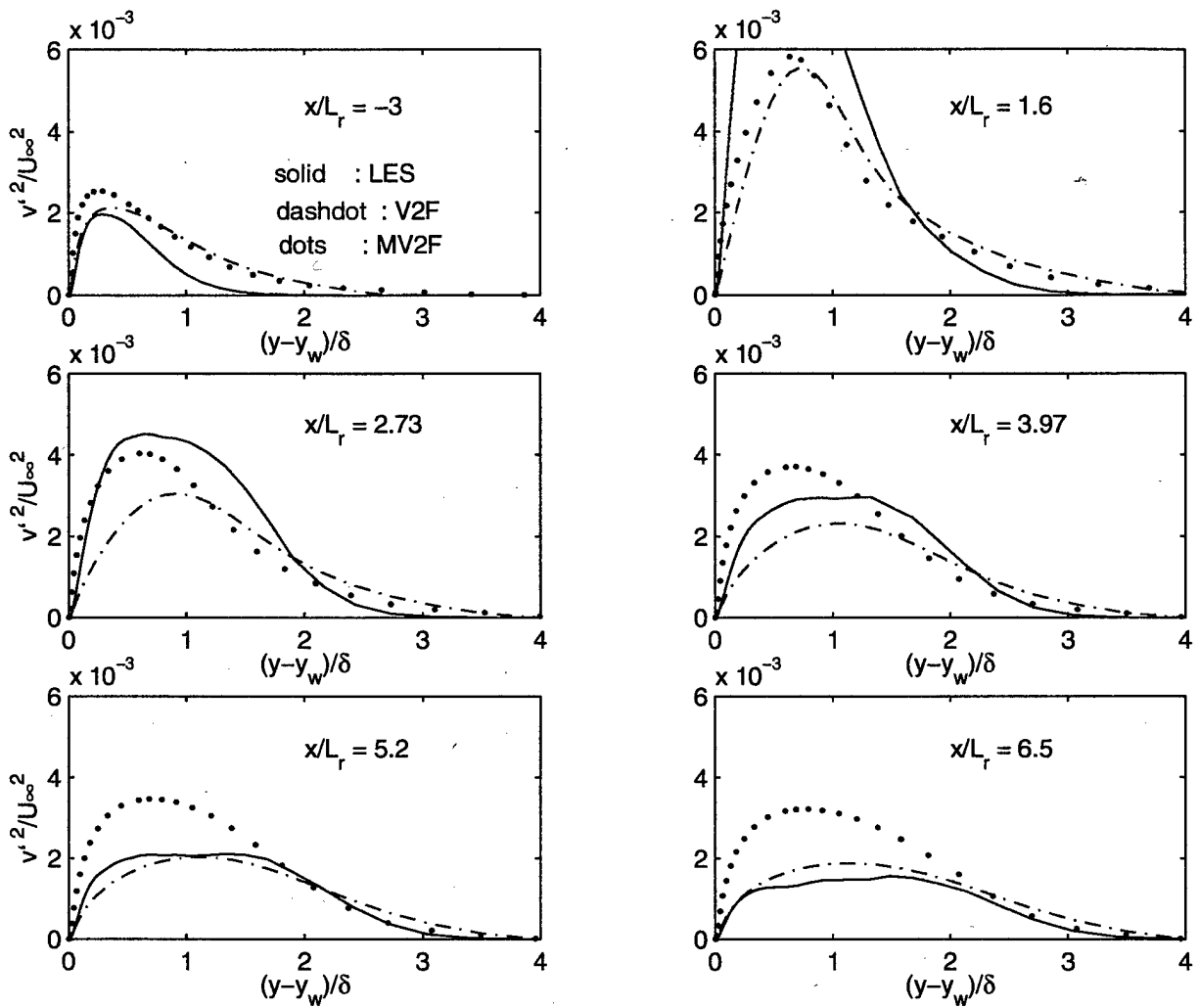


Figure 18: Normal stress  $v'^2/U_\infty^2$  in the wall normal direction at  $x/L_r = -3, 1.6, 2.73, 3.97, 5.2, 6.5$ ; solid: LES, dashdot: V2F, dots: MV2F.

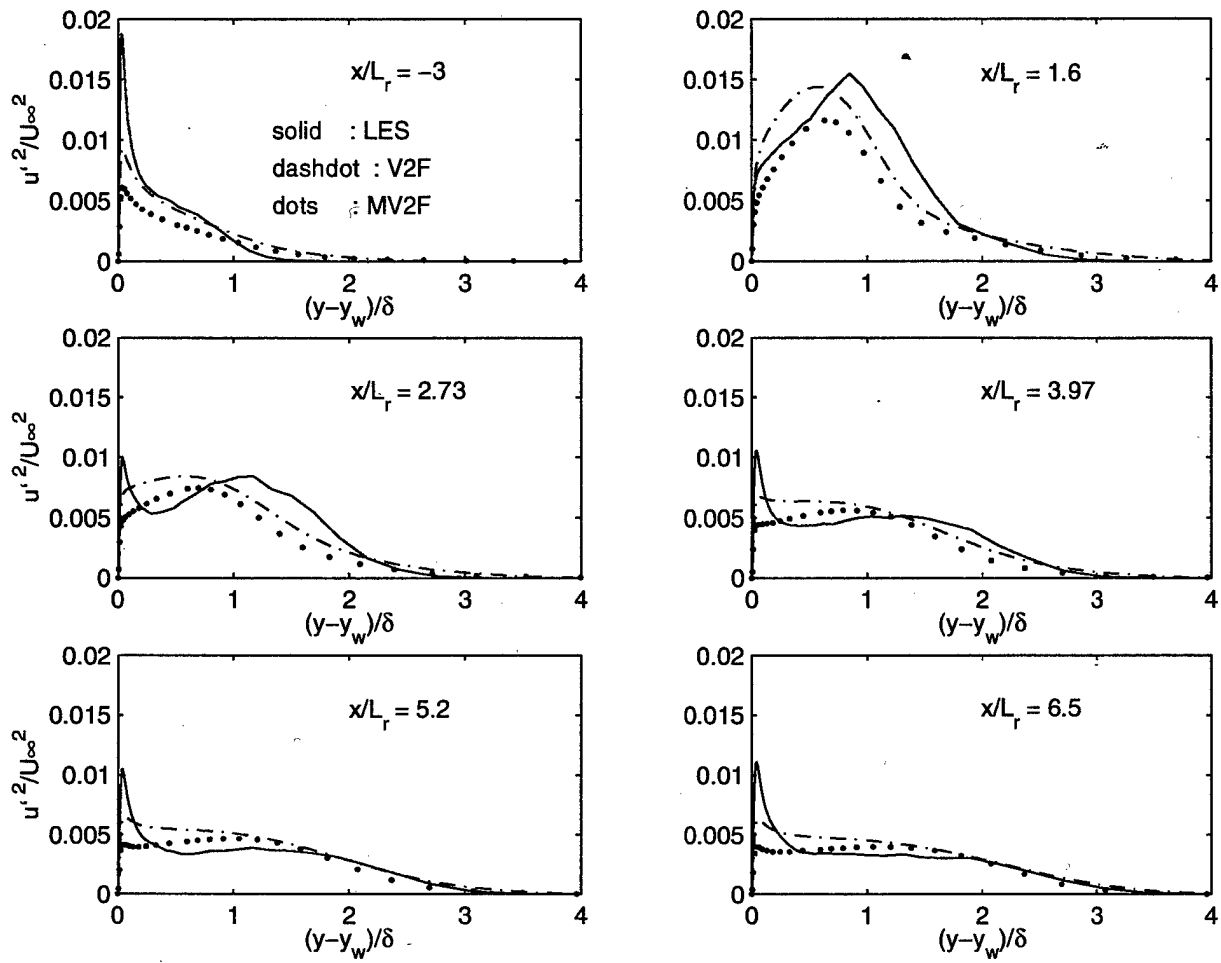


Figure 19: Normal stress  $u'^2/U_\infty^2$  in the wall normal direction at  $x/L_r = -3, 1.6, 2.73, 3.97, 5.2, 6.5$ ; solid: LES, dashdot: V2F, dots: MV2F.

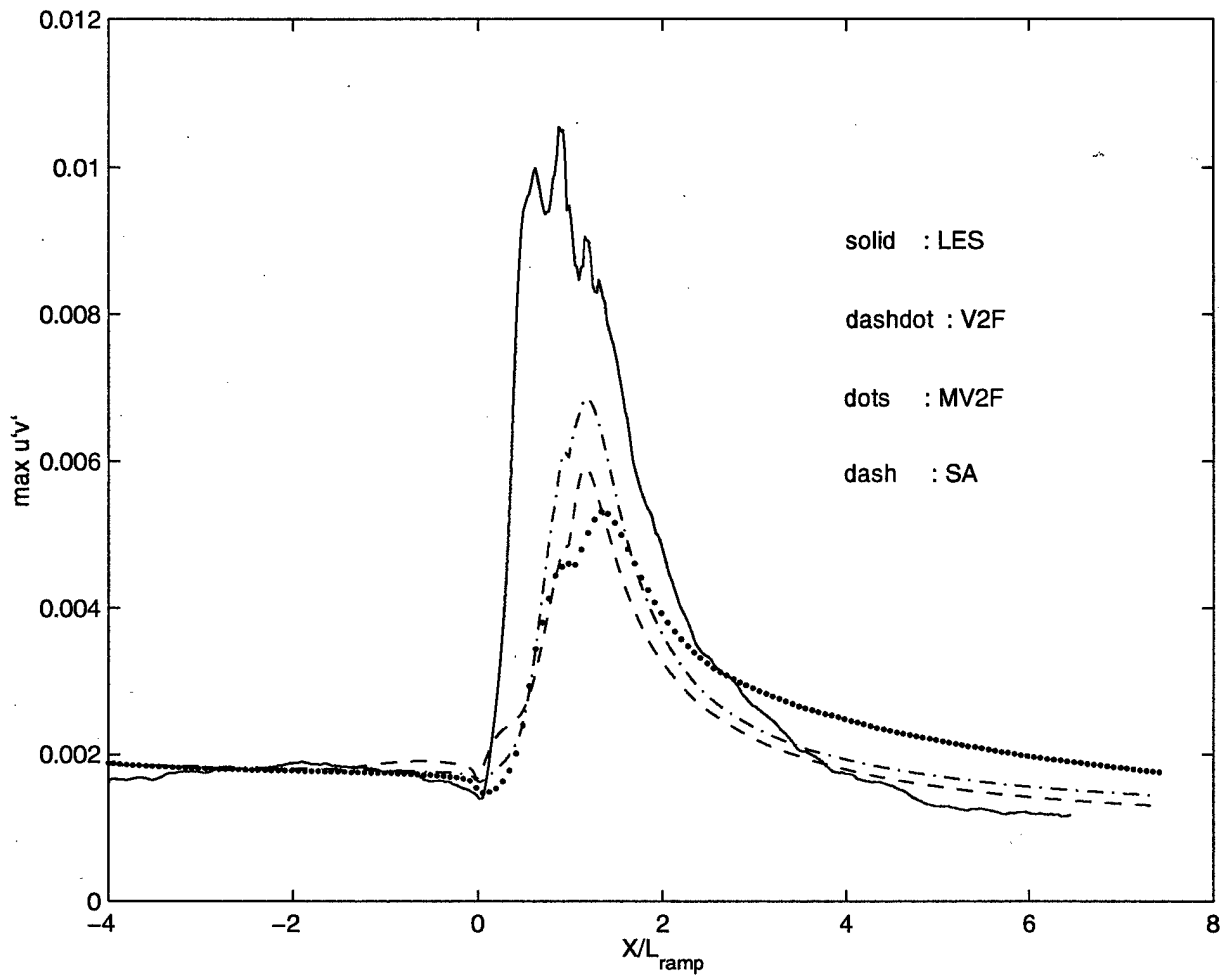


Figure 20: Local maxima of  $u'v'/U_{\infty}^2$  in the streamwise direction; solid: LES, dashdot: V2F, dots: MV2F.

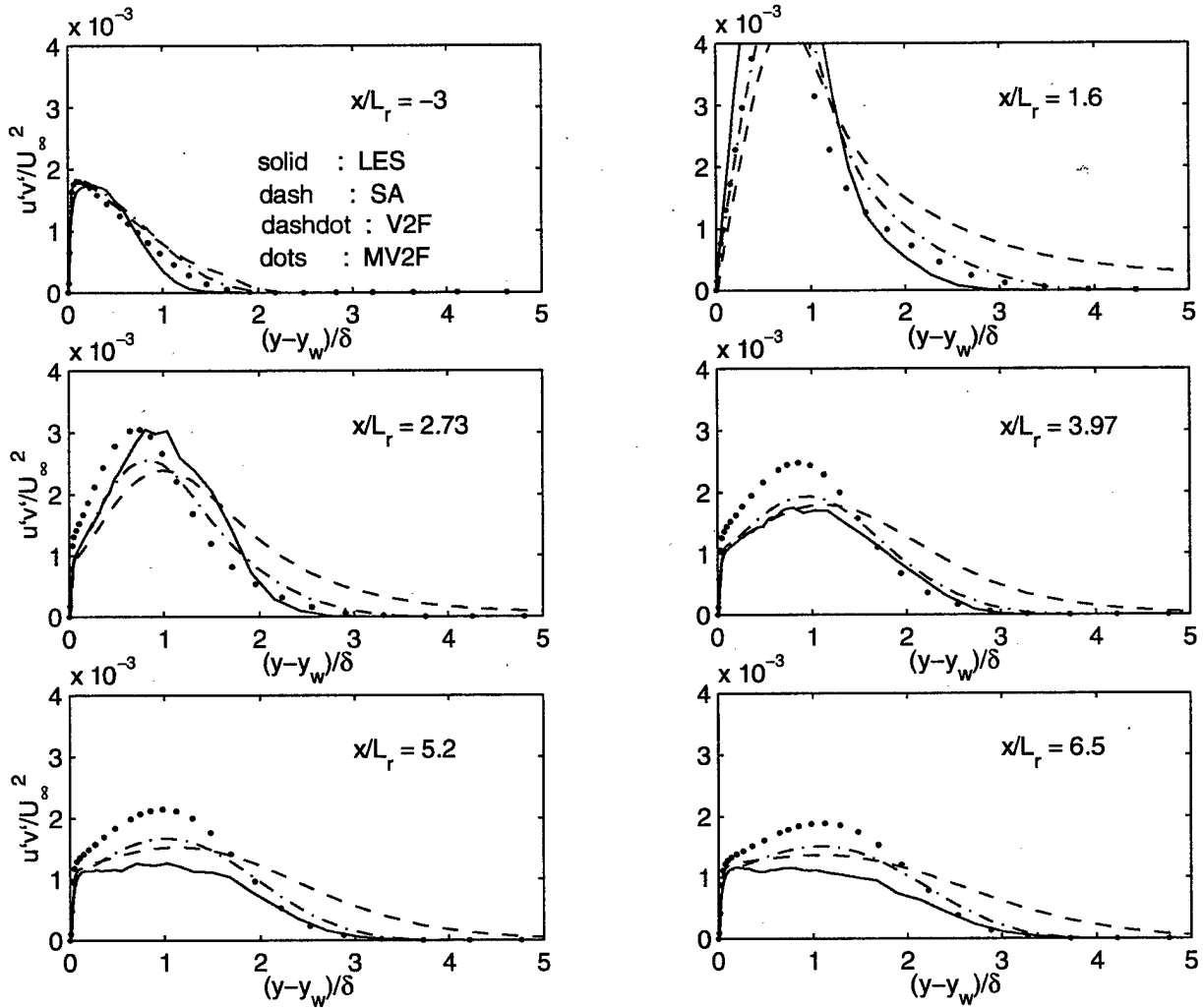


Figure 21: Reynolds shear stress  $u'v'/U_\infty^2$  at  $x/L_r = -3, 3.97, 5.2, 6.5$ ; solid: LES, dashdot: V2F, dots: MV2F.

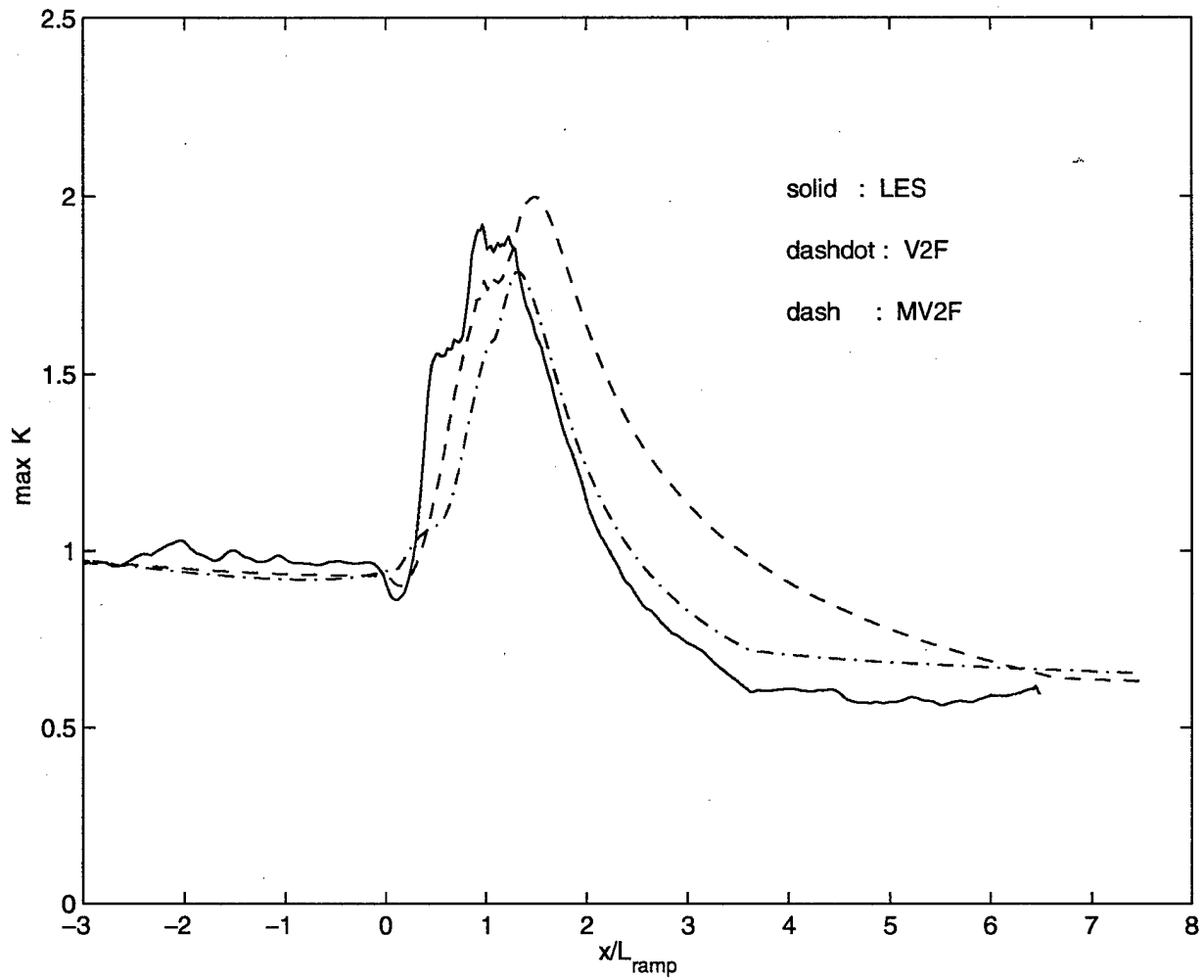


Figure 22: Local maxima of turbulent kinetic energy in the streamwise direction; solid: LES, dashdot: V2F, dash: MV2F.

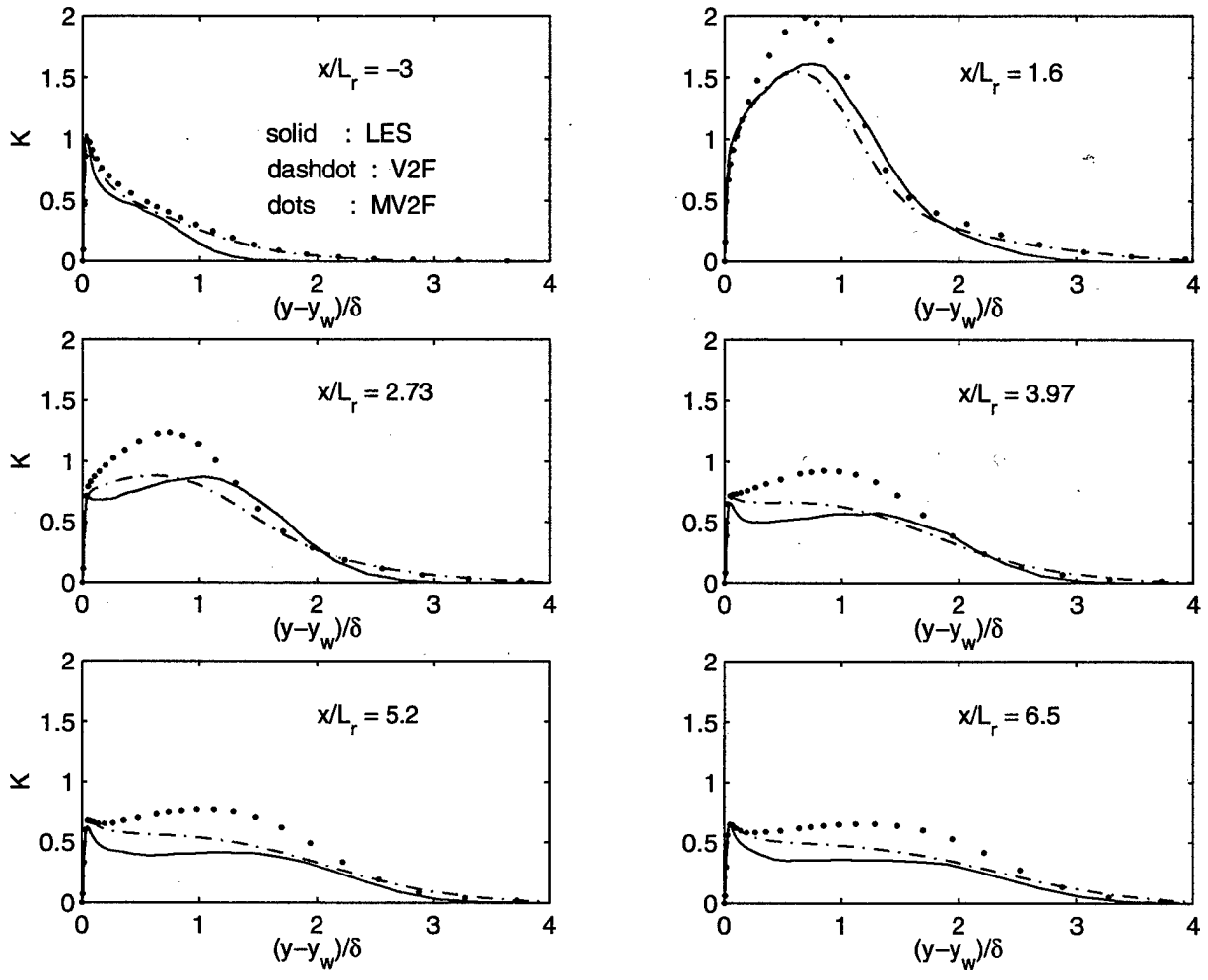


Figure 23: Turbulent kinetic energy in the wall normal direction at  $x/L_r = -3, 1.6, 2.73, 3.97, 5.2, 6.5$ ; solid: LES, dashdot: V2F, dots: MV2F.

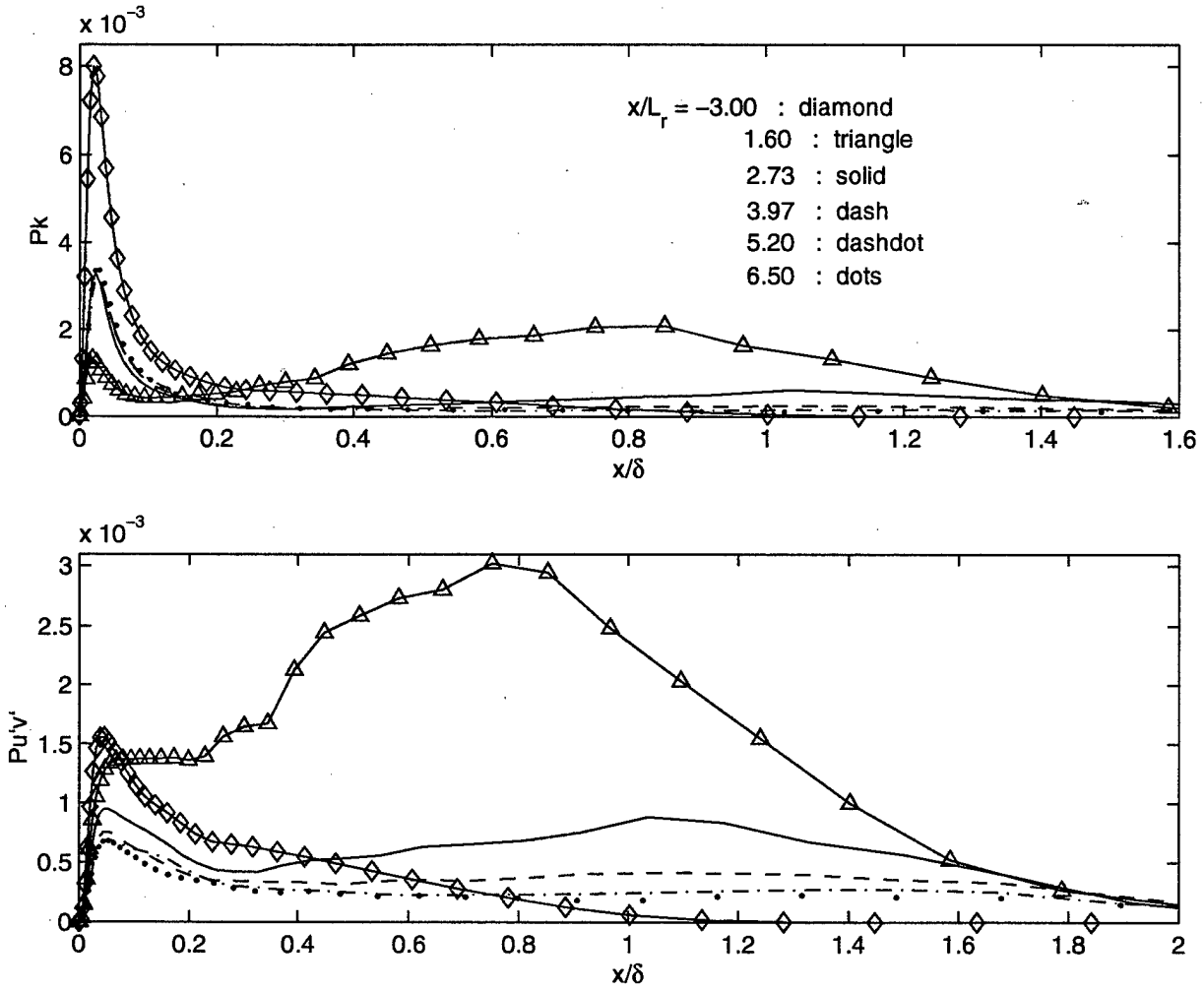


Figure 24: Upper frames: production of turbulent kinetic energy,  $-\overline{u'v'}(\partial\overline{U}/\partial y + \partial\overline{V}/\partial x) + (\overline{u^2} - \overline{v^2})\partial\overline{V}/\partial y$ , at  $x/L_r = -3$  (diamond), 1.6 (square), 2.73 (solid), 3.97 (dash), 5.2 (dashdot) and 6.5 (dots). Lower frames: production of turbulent shear stress,  $\overline{u^2}\partial\overline{V}/\partial x + \overline{v^2}\partial\overline{U}/\partial y$  with symbols denote the same as above.

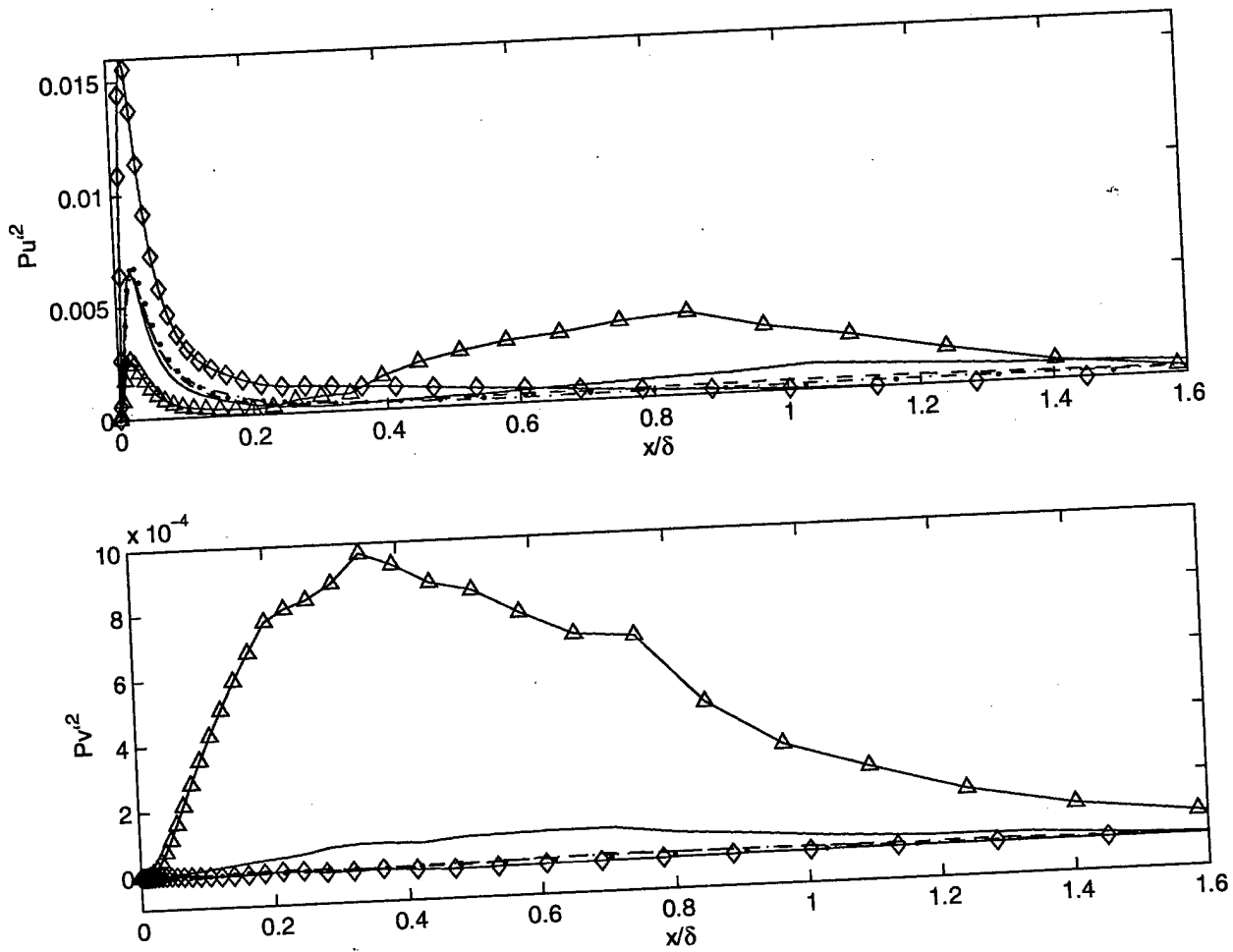


Figure 25: Production of Reynolds stress  $u^2$ ,  $2(\overline{u^2} \partial \overline{V} / \partial y - \overline{u'v'}) \partial \overline{U} / \partial y$  (above) and production of Reynolds stress  $v^2$ ,  $-2(\overline{v^2} \partial \overline{V} / \partial y + \overline{u'v'}) \partial \overline{V} / \partial x$ . Symbols denote the same as in fig. 24.